Optimal Operation of Batch Enantiomer Crystallization: From Ternary Diagrams to Predictive Control

Caio Felippe Curitiba Marcellos
Programa de Engenharia Química - COPPE, Universidade Federal do Rio de Janeiro, Rio de Janeiro,
RJ 21941-914, Brazil

Helen Durand
Dept. of Chemical and Biomolecular Engineering, University of California, Los Angeles, CA 90095-1592

Joseph Sang-Il Kwon [ID]
Department of Chemical Engineering, Texas A&M University, College Station, TX 77840

Amaro Gomes Barreto Jr.
Escola de Química, Universidade Federal do Rio de Janeiro, Rio de Janeiro,
RJ 21941-909, Brazil

Paulo Laranjeira da Cunha Lage [ID]
Programa de Engenharia Química - COPPE, Universidade Federal do Rio de Janeiro, Rio de Janeiro,
RJ 21941-914, Brazil

Maurício Bezerra de Souza Jr.
Escola de Química, Universidade Federal do Rio de Janeiro, Rio de Janeiro, RJ 21941-909, Brazil

Argimiro Resende Secchi [ID]
Programa de Engenharia Química - COPPE, Universidade Federal do Rio de Janeiro, Rio de Janeiro,
RJ 21941-914, Brazil

Panagiotis D. Christofides [ID]
Dept. of Chemical and Biomolecular Engineering and Dept. of Electrical Engineering, University of California,
Los Angeles, CA 90095-1592

In this work, the modeling and control of batch crystallization for racemic compound forming systems is addressed in a systematic fashion. Specifically, a batch crystallization process is considered for which the initial solution has been pre-enriched in the desired enantiomer to enable crystallization of only the preferred enantiomer. A method for determining desired operating conditions (composition of the initial pre-enriched solution and temperature to which the mixture must be cooled for maximum yield) for the batch crystallizer based on a ternary diagram for the enantiomer mixture in a solvent is described. Subsequently, it is shown that the information obtained from the ternary diagram, such as the maximum yield attainable from the process due to thermodynamics, can be used to formulate constraints for an optimization-based control method to achieve desired product characteristics such as a desired yield. The proposed method is demonstrated for the batch crystallization of mandelic acid in a crystallizer with a fines trap that is seeded with crystals of the desired enantiomer. The process is controlled with an optimization-based controller to minimize the ratio of the mass of crystals obtained from nuclei to the mass obtained from seeds while maintaining the desired enantioseparation. © 2017 American Institute of Chemical Engineers AIChE J, 64: 1618–1637, 2018
Keywords: crystallization, enantiomeric separation, ternary diagram, batch crystallization control, model predictive control, population balance models

Introduction

A variety of useful molecules occur as chiral compounds, or compounds for which two nonsuperimposable chemical structures that are mirror images of one another (referred to as left- and right-handed enantiomers) exist although their chemical composition is the same. For example, the components of

Table 1. Enantiomers-Based Drugs with Different Biological Effects

Compound	Active Enantiomer Effect	Counter Enantiomer Effect
Ethambutol[4]	Tuberculosis treatment	Causes blindness
Naproxen[5]	Treats arthritis pain	Liver damage
Methorphan[6]	Cough suppressant	Narcotic analgesic
Methamphetamine[7]	Nasal decongestant	Central nervous system stimulant
Praziquantel[8]	Treats schistosomiasis	Bitter taste

many drugs are chiral molecules.[1] For many chiral compounds used in pharmaceuticals, the enantiomers of that compound have different biological activities (e.g., pharmacology, toxicology, pharmacokinetics, and metabolism), despite having the same chemical composition.[2,3] Examples of substances in which these differences are well-known are described in Table 1. Therefore, the separation of enantiomers has great appeal as a topic in research and technology development.[3,9–11]

Two major approaches for enantiomeric separation are asymmetric synthesis and chiral resolution. Although the former technology has progressed significantly, it still has limited application, or it may have a prohibitive cost.[12–14] Thus, chiral resolution methods are in development to achieve cost-effective, reliable and flexible enantioselective separation processes (for a detailed review of both approaches see Ref. 14). A technique for obtaining a pure enantiomer that falls within the chiral resolution category is crystallization, which is an important technological process for forming particles in the pharmaceutical industry and has a fundamental role in drug properties such as stability, processing, and toxicity, which can be affected by crystal properties such as the structure, particle-size distribution, and purity.[15,16]

Enantiomers are commonly classified into three types based on the binary melting diagram for a solution of the enantiomers: (1) racemic compounds (in the solid phase, crystals are formed containing both enantiomers in the same unit cell); (2) racemic conglomerates (in the solid phase, crystals of each pure enantiomer form and are mechanically mixed) and (3) pseudoracemates (in the solid phase, crystals are formed containing both enantiomers but with a somewhat random order). Racemates, or racemic mixtures, contain equal amounts of left- and right-handed enantiomers. Further information and details on the types of enantiomers based on phase diagrams is provided by.[17,18]

It is estimated that about 90% of all enantiomeric systems belong to the racemic compound group.[18] As a result, research on methods for enantioseparation for this group is of great interest. Several crystallization-based enantioseparation methods exist, including conversion of the enantiomers to diastereomers and crystallizing the diastereomers, and crystallization in the presence of an optically active solvent. However, such techniques require additional materials (e.g., resolving agents or optically active solvents) with specific features. The advantage of direct crystallization (without agents that promote optical changes) is the fact that it is a simple and economical technique performed with standard equipment.[14]

For a racemic compound forming system at racemate liquid composition (equal mass fractions of both enantiomers), the solid phase formed on cooling will be the racemic compound. To form the desired pure enantiomer solid, the liquid must be enantiomerically enriched in the desired enantiomer before cooling. Enrichment can be obtained by separation operations such as simulated moving bed (SMB) chromatography, which in recent years has gained importance for the separation of enantiomers due to factors such as better characterization of design. The coupling of chromatography with direct crystallization can allow a pure enantiomer to be obtained in solid form by the crystallization process, while allowing the chromatography process to operate with high productivity without requiring high purities of the desired enantiomer in the effluent.[14,19] One of the pioneers of coupling a chromatographic method with crystallization was Ref. 20 to obtain a single enantiomer of praziquantel.

Several studies have been performed in the analysis of the coupled simulated moving bed (SMB) chromatography-crystallization process for enantioseparation (e.g., Ref. 21–25) However, study of optimal control for a batch direct enantioselective crystallization process is scarce. Although a number of results on crystallization utilizing the optimization-based control design model predictive control (MPC) have appeared in the literature (e.g., Ref. 26, 27) to the best knowledge of the authors, no results on MPC for crystallization of a racemic compound forming system have appeared. The unique thermodynamic properties of racemic compound forming systems in solvent establish process constraints different from those observed in other works involving crystallization and MPC that can be explicitly addressed with a well-designed MPC. The MPC could also seek to operate the process in a manner that achieves the highest pure enantiomer crystal yield possible while minimizing the ratio of the mass of crystals from nuclei to the mass of crystals from seeds during batch crystallization. Thus, this work focuses on analyzing the batch crystallization process using the ternary diagram, on modeling of the process with and without a fines dissolution loop, and on the development of an MPC-based control approach. More specifically, the ternary diagram, a common chemical engineering tool for presenting solution thermodynamics information (e.g., Ref. 28) provides the information required to determine the batch operating conditions, controller constraints, and controller model (e.g., the saturation composition predictions required for nucleation and growth rate modeling throughout the batch) to determine optimal control actions with a model predictive control strategy when the solution thermodynamic data meets certain assumptions. The operation and control strategy are demonstrated throughout the work using the mandelic acid (MA) in water system as it is widely used in the literature as a model system and the kinetic and solid–liquid equilibrium data for this process is available in the literature. Given the batch nature of the process, the use of control methods addressing stabilization to a steady-state (or set-point) are not appropriate for this process (this issue is further addressed in Remark 4 below).

Batch Crystallization Operation and Control Design for Racemic Compound Forming Systems Using the Ternary Diagram

This section presents a systematic method for controlling a batch crystallization process for a racemic compound forming system with model predictive control to obtain crystals of a single desired enantiomer when the solution being crystallized is assumed to be enriched in the desired enantiomer through a separation operation (e.g., SMB chromatography) prior to the batch crystallization. The process model utilized within the

MPC and the operating strategy developed to be enforced by the MPC are based on solution thermodynamics information, visually displayed in a ternary diagram, in particular the saturation composition as a function of temperature and limitations on the crystallization process (yield and operating temperatures) based on thermodynamic limitations of crystallization of a single pure enantiomer. The next two sections build to the presentation of the systematic modeling, operation, and control strategy in the third section by introducing the framework necessary for assessing the saturation composition as a function of temperature and the theoretical crystallization/yield limitations that will be exploited within the control design.

Saturation composition equations based on a ternary diagram

As noted in the "Introduction" section, it is desirable to obtain many useful chiral products as a single pure enantiomer, and therefore, the batch crystallization operation and control strategy developed in this work will seek to produce crystals of a single desired enantiomer referred to as the R enantiomer or R in this manuscript (the counter will be referred to as the S enantiomer or S) from a mixture of both enantiomers and a solvent (which can also be a mixture). Solution thermodynamics indicates that this operating objective can only be achieved within a specific range of operating conditions (liquid-phase compositions and temperatures). Specifically, at a given temperature, depending on the composition of the mixture, a racemic compound forming system in a solvent may form one of six different phase combinations: a liquid solution, a liquid solution in equilibrium with pure enantiomer R, a liquid solution in equilibrium with pure enantiomer S, a liquid solution in equilibrium with a solid racemic compound, a liquid solution in equilibrium with the solid racemic compound and pure R, or a liquid solution in equilibrium with the solid racemic compound and pure S.[19] A ternary diagram (in right or equilateral triangle form;[17] details on converting between these forms can be found in Part A of the Supporting Information) provides a visual representation of the operating conditions which correspond to each of these six phases at a given temperature.

An example ternary diagram (in right triangle form) for a racemic compound forming system (in this case, MA in water) is presented in Figure 1. The x and y axes are labeled with the mass fractions w_R and w_S of the R and S enantiomers in the liquid phase solution. The bold line with a slope of -1 extending from $w_S = 1.0$ to $w_R = 1.0$ represents a line along which the mass fraction $w_W = 1 - w_S - w_R$ of solvent (water) in the liquid mixture is zero (a mixture of enantiomers only). The dashed line with a slope of 1 that passes through the origin corresponds to the racemic composition. Although this diagram could be partitioned into six regions reflecting the six possible phases of the racemic compound forming system, only the two-phase region in which the liquid solution is in equilibrium with solid R (the region of interest for the batch crystallization process) is delineated (for the full description of the ternary diagram for a racemic compound forming system, the reader is referred to Ref. 17, 29). As the temperature changes, the boundaries of each of the six phase regions change within the ternary diagram. This is exemplified for the two-phase region of interest at three different temperatures in Figure 1. At temperature T_0, the two-phase region is represented by the region within triangle **BER**, at T_1 it is the region within triangle
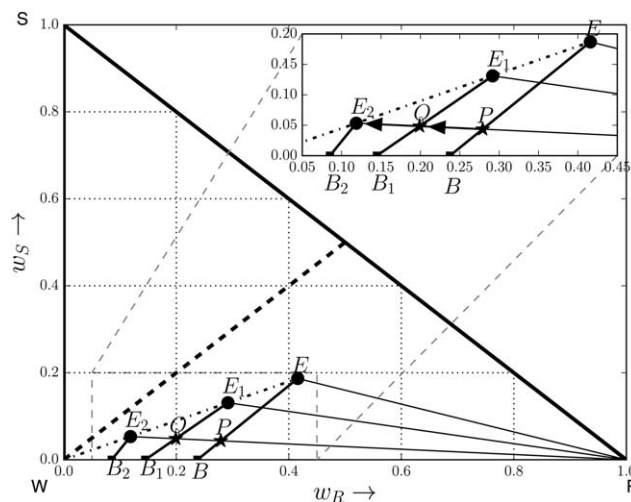

Figure 1. Ternary diagram in right triangle form for an example racemic compound forming system (mandelic acid in water).

Only the two-phase region in which solid R is in equilibrium with a saturated solution is presented for three different temperatures. Points R, S, and W signify the compositions on the ternary diagram corresponding to pure R, S, and W, respectively. A zoomed-in version of several compositions on the diagram is presented in the upper right corner for better visualization. The dashed-dotted line represents a line of constant eutectic purity. The dashed line with a slope of 1 represents the racemic composition.

B_1E_1R, and at T_2 it is the region within triangle B_2E_2R. In Figure 1, E, E_1, and E_2 are the eutectic compositions at temperatures T_0, T_1, and T_2 respectively, with $T_2 < T_1 < T_0$ (a eutectic composition is a composition which corresponds to the lowest temperature to which one can cool a solution with an initial composition in the two-phase region without forming a racemic solid, as will be discussed further below). B, B_1, and B_2 are the binary saturation compositions at temperatures T_0, T_1, and T_2 (the binary saturation composition refers to the composition of a mixture without the counter enantiomer, i.e., only R and solvent). The lines $\overline{EB}$, $\overline{E_1B_1}$, and $\overline{E_2B_2}$ represent the solubility lines for the pure enantiomer R at temperatures T_0, T_1, and T_2, respectively.

When the composition of a liquid mixture falls within the two-phase region (for example, point **P** when the temperature is T_1 is within the two-phase region represented by the triangle B_1E_1R), this liquid mixture is not at thermodynamic equilibrium and will separate into two phases (a saturated liquid in equilibrium with pure solid R) if allowed to come to thermodynamic equilibrium. For example, at T_1, a liquid mixture with initial composition **P** will separate into two phases with compositions on the line $\overline{RP}$. The saturated liquid will have a composition corresponding to the intersection of line $\overline{RP}$ with the solubility line at the given operating temperature ($\overline{E_1B_1}$); this means that the saturated liquid will have the composition described by **Q**. When the temperature of the solution drops, the two-phase region changes, and a composition that used to be at thermodynamic equilibrium will fall within the two-phase region (e.g., a solution with composition **P** is at thermodynamic equilibrium at T_0 but is within the two-phase region if the temperature drops to T_1). Therefore, though the solution with composition **P** at T_0 is saturated and thus there is no driving force for crystallization, it is supersaturated at T_1 and can

crystallize until it reaches the new solubility line $\overline{\mathbf{E_1B_1}}$. Upon cooling of a liquid mixture during the crystallization process, the saturation composition will move along the line $\overline{\mathbf{RP}}$.

We seek to utilize the ternary diagram to obtain an expression for the saturation composition as a function of temperature. The first step in this derivation for the systems that we consider in this work is to determine equations for line $\overline{\mathbf{RP}}$ and for the solubility curve at a given temperature; the second step is to determine the composition at which they intersect, which corresponds to the saturation composition at that temperature. The composition of R along line $\overline{\mathbf{RP}}$ (denoted by $w_R^{\overline{\mathbf{RP}}}$) can be represented in terms of the mass fractions of R and S corresponding to the initial composition at point $\mathbf{P}$ ($w_R^{\mathbf{P}}$ and $w_S^{\mathbf{P}}$, respectively) and the mass fraction of S along the line $\overline{\mathbf{RP}}$ (denoted by $w_S^{\overline{\mathbf{RP}}}$) as follows (the derivation of this relationship utilizing mass balances is provided in Part B of the Supporting Information)

$$w_R^{\overline{\mathbf{RP}}} = \frac{w_R^{\mathbf{P}}-1}{w_S^{\mathbf{P}}} w_S^{\overline{\mathbf{RP}}} + 1 \tag{1}$$

When no experimental solubility data is available, approximations of the solubility information may be obtained using the Schroeder-Van Laar equation.[17,19,31] Experimental solubility data can be used to indicate the shape of the solubility curves. For MA in water, experimental solubility data indicates that the solubility curve can be approximated by a straight line that extends from the binary saturation composition to the eutectic composition, which contributes to the triangular-shaped two-phase regions in Figure 1.[19] At a given temperature, when the solubility curve can be represented by a line on the right triangle ternary diagram connecting the eutectic and binary saturation compositions at the given temperature, compositions $(w_R^{E_c}, w_S^{E_c})$ representing the mass fractions of R and S at the eutectic composition and $(w_R^{B_s}, w_S^{B_s})$ representing the mass fractions of R and S at the binary saturation composition for a given temperature T can be used to form the point-slope form of the equation for the mass fraction of R along the line connecting the binary saturation composition and eutectic composition at the given temperature. For example, the composition along the solubility line $\overline{\mathbf{E_1B_1}}$ at T_1 for MA in water is given by

$$w_R^{\overline{\mathbf{E_1B_1}}} = \frac{w_R^{\mathbf{E_1}}-w_R^{\mathbf{B_1}}}{w_S^{\mathbf{E_1}}-w_S^{\mathbf{B_1}}} w_S^{\overline{\mathbf{E_1B_1}}} + \left[w_R^{\mathbf{B_1}} - \frac{w_R^{\mathbf{B_1}}-w_R^{\mathbf{E_1}}}{w_S^{\mathbf{B_1}}-w_S^{\mathbf{E_1}}} w_S^{\mathbf{B_1}} \right] \tag{2}$$

For the systems that we consider in this work, when formulas for the solubility curve and the line including $\mathbf{R}$ and the initial composition $\mathbf{P}$ are determined at a given temperature (e.g., Eqs. 1–2 for T_1 in Figure 1), their intersection can be used to determine the composition (w_R^{sat}, w_S^{sat}, w_W^{sat}) of the liquid in equilibrium with pure R given the initial liquid composition at this temperature (the equations can be further simplified by setting $w_S^{\mathbf{B_1}}=0$ by definition of the binary saturation composition). Furthermore, if relations have been obtained from experimental data for the R and S enantiomer binary saturation composition ($w_R^{B_s}$ and $w_S^{B_s}$) and eutectic composition ($w_R^{E_c}$ and $w_S^{E_c}$) as functions of temperature (T) only, then the saturation compositions at any temperature T may be determined by finding $w_R^{B_s}(T)$, $w_R^{E_c}(T)$, $w_S^{B_s}(T)=0$, and $w_S^{E_c}(T)$ and then setting $w_R^{\text{sat}}=w_R^{\overline{\mathbf{RP}}}=w_R^{\overline{\mathbf{E_c(T)B_s(T)}}}$ and $w_S^{\text{sat}}=w_S^{\overline{\mathbf{RP}}}=w_S^{\overline{\mathbf{E_c(T)B_s(T)}}}$, where $\mathbf{E_c(T)}$ and $\mathbf{B_s(T)}$ signify the points on the right triangle ternary

diagram corresponding to compositions $(w_R^{E_c}(T), w_S^{E_c}(T))$ and $(w_R^{B_s}(T), w_S^{B_s}(T))$, respectively, to give the following

$$w_R^{sat} = \frac{\frac{w_S^{\mathbf{P}}}{w_R^{\mathbf{P}}-1} + \frac{w_R^{B_s} w_S^{E_c}}{w_R^{B_s}-w_R^{E_c}}}{\frac{w_S^{\mathbf{P}}}{w_R^{\mathbf{P}}-1} + \frac{w_S^{E_c}}{w_R^{B_s}-w_R^{E_c}}} \tag{3}$$

$$w_S^{sat} = \frac{w_S^{E_c} w_S^{\mathbf{P}}(1-w_R^{B_s})}{w_S^{E_c} - w_R^{B_s} w_S^{\mathbf{P}} + w_R^{E_c} w_S^{\mathbf{P}} - w_R^{\mathbf{P}} w_S^{E_c}} \tag{4}$$

where w_R^{sat} and w_S^{sat} in Eqs. 3–4 are now functions only of the initial composition and of temperature, and the explicit temperature dependence of $w_R^{B_s}$, $w_R^{E_c}$, and $w_S^{E_c}$ in the right-hand side of Eqs. 3–4 was not denoted for simplicity of notation. These equations can be further simplified in the special case of MA because for MA in water, the eutectic composition varies with temperature in such a way that the purity at the eutectic composition (P^e) can be modeled as a constant (independent of the temperature), where the purity is defined as

$$P = \frac{w_R}{w_R + w_S} \tag{5}$$

Therefore, given a function $w_R^{E_c}(T)$ from data, it is not necessary to also determine the function $w_S^{E_c}(T)$ from data because one can instead solve Eq. 5 for w_S at the eutectic composition to give $w_S^{E_c}(T) = \frac{1-P^e}{P^e} w_R^{E_c}(T)$ for use in Eqs. 3–4.

To demonstrate the use of Eqs. 3–4 for the MA case, we present correlations developed by Ref. 19 to correlate the R enantiomer binary saturation (w_R^B) and eutectic composition (w_R^E) with the temperature (T) in the range of 0°C to 40°C based on experimental solubility data for the MA system in water solvent from.[30] Polynomial equations were considered and the coefficients were determined by minimization of the sum of the absolute values of the relative errors. The obtained relations are as follows for T in $^\circ$C

$$w_R^{E_c}(T) = \sum_{i=0}^{4} c_{E,i}^{\text{sat}} T^i \tag{6}$$

$$w_R^{B_s}(T) = \sum_{i=0}^{5} c_{B,i}^{\text{sat}} T^i \tag{7}$$

with the estimated coefficients $c_E^{\text{sat}} = [c_{E,0}^{\text{sat}}\ c_{E,1}^{\text{sat}}\ c_{E,2}^{\text{sat}}\ c_{E,3}^{\text{sat}}\ c_{E,4}^{\text{sat}}]^T$ $= [5.6939 \cdot 10^{-2}, 2.6283 \cdot 10^{-3}, -2.4289 \cdot 10^{-4}, 1.6516 \cdot 10^{-5}, -1.6197 \cdot 10^{-7}]^T$ and $c_B^{\text{sat}} = [c_{B,0}^{\text{sat}}\ c_{B,1}^{\text{sat}}\ c_{B,2}^{\text{sat}}\ c_{B,3}^{\text{sat}}\ c_{B,4}^{\text{sat}}\ c_{B,5}^{\text{sat}}]^T =$ $[4.4892 \cdot 10^{-2}, 2.2451 \cdot 10^{-3}, -1.3164 \cdot 10^{-4}, 1.3519 \cdot 10^{-5}, -5.3634 \cdot 10^{-7}, 8.0205 \cdot 10^{-9}]^T$. Thus, at any T, the coupling of Eqs. 6–7 with Eqs. 3–4 allows the saturation composition to be calculated for any temperature (in the 0°C-40°C range for consistency with the experimental data) and initial composition $\mathbf{P}$.

Crystallization limitations for batch operation

As a solution of enantiomers of a racemic compound in a solvent with the properties that we describe in this work is cooled, the intersection of line $\overline{\mathbf{RP}}$ with the solubility curve at the solution temperature can eventually reach the eutectic composition. Therefore, it is possible to recover more pure crystals of R from a given initial composition if the temperature is dropped until the saturation composition is reduced to the eutectic composition on the line $\overline{\mathbf{RP}}$, which is the limit for pure R crystallization (for initial composition $\mathbf{P}$ in Figure 1, e.g., this limit occurs at $\mathbf{E_2}$).

For the MA system in water, the eutectic purity is $P^e = 0.69$,[29] and the line with purity P^e through the eutectic compositions at all temperatures is represented by line $\overline{\mathbf{WE}}$ in the ternary diagram of Figure 1 due to the form of Eq. 5, which has no dependence on the solvent mass fraction. A line of constant purity P can be represented in Figure 1 as a line extending from the origin to the point with $w_R = P$ on the bold line of slope -1 connecting $w_S = 1$ and $w_R = 1$ in Figure 1 (because this bold line represents a solution of only w_R and w_S, so the denominator of Eq. 5 is 1 along this line, and the purity is equal to the value of w_R at each point along this line). At a given temperature, pure R will crystallize only if the purity of the initial solution is higher than P^e within the two-phase region.[19] When the eutectic purity of an enantiomeric solution can be modeled as constant regardless of temperature as for mandelic acid in water,[19] the eutectic composition representing the limit for pure R crystallization for a given initial composition $\mathbf{P}$ can be determined from the intersection of line $\overline{\mathbf{RP}}$ with the line of purity P^e ($\overline{\mathbf{WE}}$).

The thermodynamic limitations on crystallization impact the crystal yield Y_c, defined as the ratio of the mass of solid R that is crystallized during batch operation to the mass of R initially present in the liquid phase, that can be obtained from a solution with a given initial purity and is given by

$$Y_c = \frac{P^i - P^f}{P^i(1 - P^f)} \qquad (8)$$

Equation 8 provides the yield at the end of a batch operation as a function of initial and final purities P^i and P^f, respectively (i.e., the initial purity from the pre-enrichment process is defined as $P^i = \frac{w_R^i}{w_R^i + w_S^i}$, where w_R^i and w_S^i represent the mass fractions of R and S in the feed to the crystallizer (which may be different than their values in the outlet of the pre-enrichment process if solvent was added or removed before the pre-enrichment process outlet entered the crystallizer; such addition or removal of solvent, however, would not affect the purity of the liquid), and P^f is defined analogously). The relation in Eq. 8 is obtained using mass balances in a manner analogous to that presented for a continuous crystallization process in Ref. 19 and is derived in Part C of the Supporting Information.

Furthermore, the mass fraction of R at the end of the batch (w_R^f) depends only on the initial mass fraction of R and the initial and final purities as follows

$$w_R^f = \frac{(P^f P^i - P^f)w_R^i}{(P^i - P^f)w_R^i + P^f P^i - P^i} \qquad (9)$$

Batch crystallization operation and controller design using ternary diagram data

In this section, we combine the results of the last two sections to develop a systematic procedure for modeling, operation, and control of a batch crystallization process for a racemic compound forming system that has been pre-enriched in the desired enantiomer. The first step in the operating procedure is the determination of the initial operating temperature and composition. The choice of these conditions relies on the initial purity from the pre-enrichment process and the desired working temperature range.

For a given P^i, Eq. 5 shows that the ratio of w_R to w_S is fixed, but that the actual values of w_R and w_S can vary because the purity does not specify the solvent mass fraction.

Replacing $w_R + w_S$ with $1 - w_W$ in Eq. 5, the mass fraction of the desired enantiomer is a function of the solvent mass fraction for a given purity P as follows: $w_R = P(1 - w_W)$. Thus, when the initial purity is fixed by the pre-enrichment process, the initial composition can be readily adjusted by solvent evaporation or diluting with additional solvent before starting the batch; however, the exact value to which to adjust the initial composition depends on the desired operating temperature range.

The lower bound on the desired operating temperature range is fixed by solution thermodynamics. In particular, Eq. 8 implies that for a given P^i, the greatest yield of crystals of pure R will be obtained when P^f is as low as it can be without crystallization of S, which occurs when $P^f = P^e$ due to thermodynamic restrictions for the systems considered in this work. The temperature at which the eutectic purity P^e is reached is fixed thermodynamically by the initial mixture composition. This temperature (referred to as T_{min} in the following) can be obtained by solving

$$w_R^f - w_R^{sat}(T) = 0 \qquad (10)$$

with w_R^f given by Eq. 9 (which gives w_R^f as a function only of the final purity and initial liquid composition) and $w_R^{sat}(T)$ given by a relationship such as that developed in Eq. 3 for MA in water with relations such as those in Eqs. 6–7 that describe how the eutectic and binary saturation compositions change with temperature (with $w_S^{\mathbf{P}} = w_S^i$ and $w_R^{\mathbf{P}} = w_R^i$). Eq. 10 can be solved through an iterative method when no analytic solution exists. From the dependence of w_R^f and $w_R^{sat}(T)$ in Eq. 10 on the initial mixture composition, it is seen that the initial mixture composition directly affects the temperature T_{min} that the batch crystallizer must achieve at the end of process operation to achieve the desired yield at P^e.

When the initial mixture composition falls within the two-phase region at a given temperature, some of the mixture will crystallize unless the initial mixture composition is on the solubility line at the given temperature. Thus, it can be beneficial to initiate the batch at the saturation condition since that may avoid undesired nucleation and help the seeding control. It will also have no negative effect on the yield when P^f is fixed because according to Eq. 8, any initial composition on the line of constant purity P^i will have the same crystal yield. If it is assumed that the batch should be initiated at a saturated condition, the initial mixture composition thermodynamically sets the temperature required at the beginning of batch operation according to the following equation

$$w_R^i - w_R^{sat}(T) = 0 \qquad (11)$$

where $w_R^{sat}(T)$ is obtained in a similar manner as in Eq. 10. Thus, by fixing the final purity to a value that maximizes the yield and by initiating the batch at the saturation composition based on equilibrium considerations, the initial composition defines both the initial temperature of operation as well as the final temperature of operation. Based on the desired working temperature range, the desired initial composition can be determined for a given P^i. Considerations in selecting a working temperature range may include that all temperatures in the range can be reached in a cost-effective manner with the proposed equipment and cooling capabilities. The operating temperature range may also be chosen by considering its effect on enantiomeric system characteristics (e.g., choosing an operating temperature range that avoids undesired polymorphism or
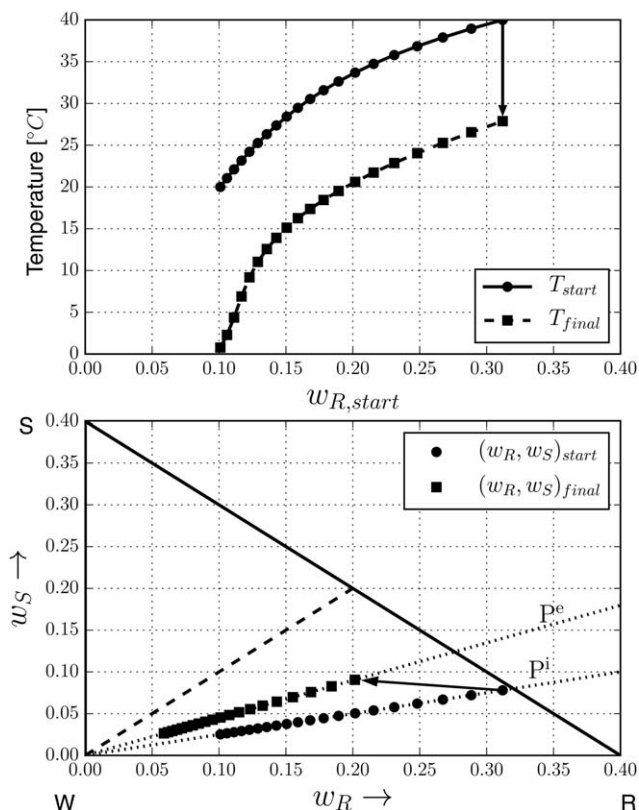
Figure 2. MA batch crystallization operation for different starting compositions $w_{R,\text{start}}$.

The bottom figure shows the starting composition (•) associated with the final composition (■) in the ternary diagram and an arrow shows that each starting temperature and initial purity corresponds to a final temperature and eutectic purity (for better visualization, only one arrow is presented). The top figure depicts the starting temperature (•) and the final temperature (■) for each starting composition considered in the bottom figure. It is noted that in the bottom figure, the bold line with a slope of -1 represents a line of constant solvent composition $w_W = 0.6$ (as only a subset of the ternary diagram data from Figure 1 is shown in this figure, the bold line with a slope of -1 does not have the same meaning in this figure as in Figure 1). The dashed line with a slope of 1 represents the racemic composition.

solvate configurations or is one in which the crystal kinetics behavior or crystal stability have been previously characterized, allowing effective process modeling).

To exemplify the choice of the initial mixture composition based on the operating temperature range, we again examine the MA case. Figure 2 shows the eutectic purity line for $P^e = 0.69$ and the line for an initial purity of $P^i = 0.80$. Figure 2 was constructed using Eqs. 10–11 with Eqs. 6 and 7 for a variety of initial compositions with purity $P^i = 0.80$. In the bottom plot in this figure, a number of circles representing various initial compositions for which $P^i = 0.80$ are plotted, as well as a number of squares representing various final compositions for which $P^e = 0.69$. The arrow signifies that a given circle corresponds to a given square in the sense that if an initial mixture with the composition signified by a circle is cooled to the eutectic point, it will reach the composition signified by the corresponding square at the eutectic point (the leftmost circle corresponds to the leftmost square, the second circle from the left corresponds to the second square from the left, and so forth). The top plot of the figure shows temperatures

corresponding to each circle and square in the bottom plot, assuming that each circle in the bottom plot represents an initial mixture composition on the saturation curve (the leftmost circle in the top figure corresponds to the leftmost circle in the bottom plot, the second circle from the left in the top plot corresponds to the second circle from the left in the bottom plot, and so forth). The temperatures are plotted against $w_{R,\text{start}}$, the initial composition of the liquid mixture (assumed to be at the saturation condition). For each value of $w_{R,\text{start}}$, the temperature corresponding to saturation for the given $w_{R,\text{start}}$ is represented as a circle, and the temperature corresponding to the eutectic composition given $w_{R,\text{start}}$ is represented as a square. As in the bottom plot, the arrow indicates that a circle on a line of constant $w_{R,\text{start}}$ corresponds to a square on this same line. The top plot, then, shows the change in temperature required to go from an initial saturated solution with purity P^i to the eutectic composition representing the limit of the region of pure R crystallization associated with the initial mixture composition. The arrow shown in the top plot of Figure 2 specifically shows the temperature decrease required to crystallize a saturated solution with an initial temperature $T_{\text{start}} = 40°$C to the eutectic point. When $T_{\text{start}} = 40°$C, Eq. 11 can be solved to find the starting composition $w_{R,\text{start}}$ by solving $w_{R,\text{start}} - w_R^{\text{sat}}(T_{\text{start}}) = 0$ (and a similar equation for w_S based on Eq. 4), where $w_R^{\text{sat}}(T_{\text{start}})$ is from Eq. 3, giving $w_{R,\text{start}} = 0.31$. A final composition at $w_R^f = 0.20$ is calculated using Eq. 9 with $P^f = P^e$, which occurs at a temperature of $28.05°$C from Eq. 10. Figure 2 gives a clear indication of the operating temperature range required for a variety of initial mixture compositions with the same initial purity and allows the appropriate operating temperature range to be chosen based on the plot, which then fixes the appropriate initial composition.

MPC is proposed for operating the batch crystallization process within the desired operating temperature range because it is an optimization-based control methodology that incorporates a process model and constraints when determining control actions to apply to the process, and crystallizing a single enantiomer from a solution of two enantiomers is a thermodynamically constrained procedure (e.g., there are limitations on the range of temperatures and compositions for which crystals of a pure enantiomer will form). Composition or temperature-dependent properties in the process model used in MPC, such as the saturation composition, can be based on ternary diagram information (e.g., Eq. 3) to appropriately reflect the process thermodynamics. In addition, MPC is a flexible control design in the sense that it computes control actions that allow constraints to be met while an objective function (e.g., a function of desired crystal size properties) is optimized, resulting in a cooling trajectory for the crystallizer that, perhaps, results in higher profits or greater effectiveness of the crystals in their intended application than would be achieved by performing the crystallization with a predetermined temperature profile in the crystallizer like a linear cooling strategy. Furthermore, constraints can also be added to aid in improving the efficiency of the crystallization process, such as adding constraints on the desired yield (e.g., for the mandelic acid in water process, a constraint could be added that requires the yield at the end of the batch to reach its theoretical maximum value of Eq. 8). Furthermore, as a feedback control law, it provides a degree of robustness to disturbances and plant/model mismatch.

Because MPC calculates optimal control actions, and requires that a process model be available, it allows for closed-loop simulations to be performed to determine the most
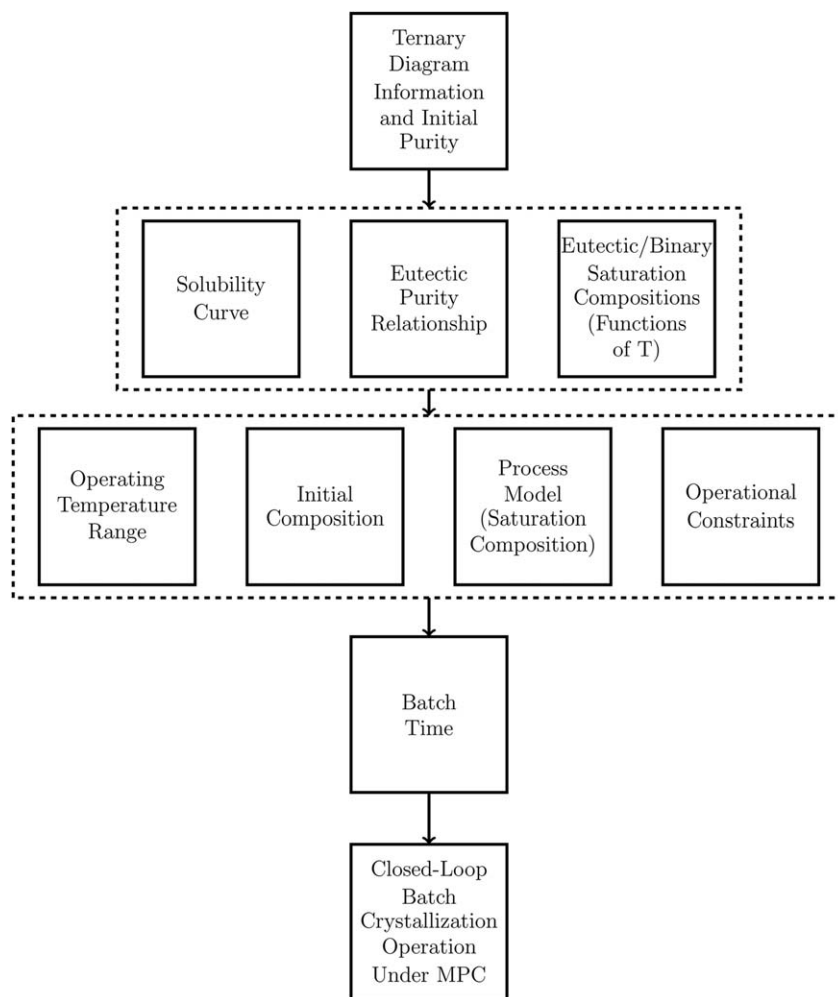
Figure 3. Schematic depicting the proposed batch modeling, operation, and control procedure.

Solution thermodynamic data including a ternary diagram and the initial purity of the solution are provided, which are then used to develop important relationships for the procedure, including equations related to the solubility curve as a function of temperature, the relationship describing the eutectic purity (e.g., $P^e = 0.69$ for mandelic acid in water), and information on the eutectic and binary saturation compositions as functions of temperature. This information is subsequently used to determine the operating conditions of the crystallizer, including the operating temperature range and initial composition, it is used in the development of the process model (e.g., by developing a relationship for the saturation composition as a function of temperature), and the development of other operational constraints such as yield constraints. This is incorporated within a model predictive control design. The length of the batch run is selected and the crystallization process is operated under the MPC with the constraints based on solution thermodynamics.

preferable final batch time for maximizing a desired objective function. MPC allows flexibility in both the constraints as well as the objective function, with the result that one or both may depend on the final batch time (e.g., requiring a desired yield to be obtained at the end of the batch). In this case, it is necessary to perform closed-loop simulations to understand the effect of the final batch time on optimizing the objective function. This is an advantage of MPC for control of enantiomeric crystallization compared to a preset cooling strategy such as linear cooling because preset strategies do not allow for optimization, feedback, or accounting for constraints, so it would be more difficult to obtain the best operating parameters for operation under such controllers.

Based on the discussion of this section, we now summarize the operation and control procedure proposed in this work for batch crystallization of a racemic compound forming system, which is summarized in Figure 3 and consists of the following steps:

Step 1. Obtain thermodynamic phase information for the racemic compound forming system (including a ternary phase diagram) and receive information on the initial purity from the pre-enrichment process.

Step 2. Develop equations for the saturation composition as a function of only the initial composition and $w_R^{E_c}(T)$ and $w_R^{B_s}(T)$ (e.g., Eqs. 3–4), and $w_S^{E_c}(T)$ if required.

Step 3. Setting both the initial and final compositions to be at saturated conditions, develop a plot like that in Figure 2 showing the various operating temperature ranges possible by varying the initial solvent composition for the given initial purity.

Step 4. Determine the desired operating temperature range and initial composition based on the plot developed in Step 3.

Step 5. Develop a batch crystallization process model to be used in an MPC formulation. The process model may depend on thermodynamic relations derived based on the ternary diagram analysis.

Step 6. Develop the constraints to be used in the MPC based on considerations for racemic compound forming systems as derived from the ternary diagram such as the desired yield (e.g., maximum yield thermodynamically possible with $P^f = P^e$ from Eq. 8 at the end of the batch) and crystallizer temperature limits.

Step 7. Run closed-loop simulations of the crystallization process under MPC with different batch times to determine the minimum batch time necessary to achieve the desired crystallization results.

Step 8. Operate the process under the proposed control strategy and adjust operating parameters or controller constraints and the model as necessary to achieve the desired yield and enantioseparation.

Several assumptions were considered to hold during the development of this operating/control procedure as follows:

ASSUMPTION 1. *The mixture under consideration is a racemic compound forming system that was pre-enriched in the desired enantiomer and for which phase equilibrium data is available at various temperatures and has the properties considered in this work (e.g., the intersection of a line through the initial composition and pure R and the solubility curve at a given temperature determines the saturation composition in the ternary diagram, and the limit of pure R crystallization occurs when this initial composition line intersects the eutectic composition at a given temperature).*

ASSUMPTION 2. *Relations for $w_R^{E_c}(T)$ and $w_R^{B_s}(T)$ (and $w_S^{E_c}(T)$ as applicable) are available.*

ASSUMPTION 3. *The initial purity P^i is fixed.*

ASSUMPTION 4. *Thermodynamic equilibrium is reached at the beginning and end of the batch.*

A key component of the proposed method is MPC for the control of direct crystallization of a racemic compound forming system, and the use of MPC in general does not depend on the assumptions but only on the availability of a process model. The required thermodynamic data for Assumptions 1 and 2 can be experimentally obtained if unavailable for a specific system. The final batch time can be adjusted to allow Assumption 4 to be met at the end of the batch (closed-loop simulations under MPC can be performed to determine a final batch time that will allow the assumption to hold). In the event that the pre-enrichment process is also being designed such that P^i is not yet fixed, the yield and operating temperature range at a variety of purities can be compared with the cost of changing the purity of the material exiting the pre-enrichment process to optimize the operating conditions of the entire process instead of only the crystallization unit. Small variations in P^i due to process disturbances between batch runs may be handled by the MPC because it incorporates feedback to provide some robustness to disturbances and plant/model mismatch, and safety factors can be used in the constraint design to prevent the cooling procedure from causing the temperature to drop to a level that would result in crystallization of the S enantiomer even in the presence of expected disturbances that cause P^i to vary.

REMARK 1. Figures 1 and 2 *were constructed using the mathematical developments of this section (Eqs. 1–11), rather than plotting experimental data points.*

REMARK 2. *There may be uncertainties or possible errors or disturbances for a given batch process that make it desirable to operate the batch crystallization until a final purity $P^f > P^e$ (despite that the greatest theoretical yield for a given P^i occurs when $P^f = P^e$ in Eq. 8) to avoid crystallization of the opposite enantiomer. In such a case, the analysis surrounding Eqs. 10–11 can still be performed, but with P^f set to the desired final purity in Eqs. 3 and 9 used to solve Eq. 10 for the temperature at the end of the batch. A purity $P^f > P^e$ may also be selected if cooling until $P^f = P^e$ requires the batch temperature to drop lower than can be achieved in a cost-effective and safe manner with the process equipment.*

REMARK 3. *The equations examined in the above sections for thermodynamic properties such as yield have focused on the MA in water process for which the solubility curve can be approximated as a straight line and the eutectic purity is independent of temperature. Linear approximations of solubility curves could be investigated for various enantiomeric systems for which the solubility curves in the equilateral ternary diagrams presented appear to be approximately linear (e.g., Tröger's base/ethanol[31] and bicalutamide/methanol[32]) and, as demonstrated in Part A of the Supporting Information, a linear solubility curve on a standard equilateral triangle ternary diagram, with pure enantiomers R and S on the base of the diagram, will result in a linear solubility curve in a right triangular representation. In the event that a nonlinear solubility curve provides a better representation of the thermodynamic data and Assumption 1 is met, Eq. 2 can be replaced with equations that approximate the phase boundaries through nonlinear functions of $w_R^{E_1}$, $w_R^{B_1}$, and $w_S^{E_1}$, and the procedure of finding the point of intersection of the modified solubility curve with line $w_R^{\overline{RP}}$ could give different equations for the saturation composition in Eqs. 3–4. Equations 10 and 11 could use the modified equations to extend to this case. Furthermore, when the eutectic purity is not independent of temperature and Assumption 1 is met, a potential method for extending the results of this work to that case would be to examine whether the constraints of the MPC (e.g., constraints on the yield and minimum crystallizer temperature) should reflect the value of P^f according to Eq. 5 that causes P^f to equal the value of P^e that is achieved at the temperature at which $w_R^{\overline{RP}}$ intersects both the curve for $w_R^{\text{sat}}(T)$ and the curve for $w_R^{E_c}(T)$. A correlation for $w_S^{E_c}(T)$ would also be required in this case (in addition to the correlations in Eqs. 6–7). It should also be verified that the resulting constraints do not require any safety factor (i.e., P^f greater than the determined value of P^e) to prevent the S enantiomer from crystallizing throughout the cooling process given the manner in which the eutectic purity varies throughout the cooling procedure.*

REMARK 4. *The flexibility of MPC in the constraints and the objective function enables it to be used for control of batch enantiomer crystallization. Classical stabilizing control designs for chemical processes, such as PID control, seek to drive the process state to an operating steady-state; however, for a batch process there is no steady-state, and as a result these classical control designs cannot be applied to the batch process under consideration in this work (other stabilizing control designs, such as geometric control and Lyapunov-based control, are also not applicable in this case for the same reason). Not only is MPC a viable control method for operation of batch processes, but it also offers benefits compared to other potential approaches (e.g., a pre-specified temperature trajectory within the crystallizer) because it has the ability to optimize an objective function which can be related to desired production goals which may*

be motivated by, for example, process economics, while simultaneously accounting for process thermodynamic limitations through constraints, and accounting for disturbances/ plant-model mismatch through feedback.

Batch Crystallizer Model with Fines Dissolution Loop

In the remainder of this work, the operation of a batch crystallizer for a racemic compound forming system using operating conditions and a controller design based on the ternary solid–liquid equilibrium data is exemplified through a chemical process example for mandelic acid in water. In this section, the batch crystallizer design considered for this example and the model of the crystallization process for this crystallizer design are discussed. The system is composed of a crystallizer with a jacket for temperature control and a fines dissolution tank, as depicted in Figure 4. The stream sent to the fines dissolution tank is liquid from the crystallizer that has been passed through a fines trap to filter out larger crystals of the desired enantiomer (and leave primarily fines in the stream). The fines trap in this process is not modeled as having a physical volume, and therefore, its behavior for the purposes of process modeling is like the behavior of a filter between the crystallizer volume and the stream leaving the crystallizer. The fines dissolution loop scheme was considered since it is a widely used strategy to enhance crystal growth while reducing the total number of particles in the system.[33] Though material is exchanged between the crystallizer and the fines dissolution tank, the overall system comprised of both of these tanks is closed, so the operation is a batch operation.

The following modeling assumptions are made in the development of mass, energy, and population balances for the crystallization process:

- The internal coordinates of the crystal particles can be represented only by the crystal characteristic size l;
- Both the crystallizer and fines dissolution tank are assumed to be well-mixed;
- Both the liquid (solvent with dissolved S and R enantiomers) and solid crystal R in the crystallizer and fines dissolution tank are assumed to have constant densities;
- The liquid in the crystallizer is assumed to have a constant heat capacity;
- Crystal breakage and aggregation is neglected;
- The crystal nucleation and growth kinetics can be expressed by empirical correlations;
- Only pure R enantiomer is crystallized (no S enantiomer or solvent takes a crystal form).

These assumptions are consistent with standard chemical engineering and crystallization modeling practices in the literature.[34–38]

The crystal size distribution can be described by the well-established population balance equation, which for a batch process with fines removal takes the form

$$\frac{\partial n}{\partial t} = -\frac{\partial}{\partial l}(Gn) + B_0 \delta(l-l_0) - n\frac{d}{dt}\ln m_W$$
$$+ \frac{1}{m_W}\left[n_{in}\dot{m}_{W,in} - n_{out}\dot{m}_{W,out}\right]$$
(12)

where l_0 is the minimum stable characteristic crystal size (here considered to be zero), B_0 represents the nucleation rate, G is the growth rate and $n = n(t, l)$ is the particle-size distribution (PSD) dependent on characteristic size l and time t. $\delta(l-l_0)$ is the Dirac delta function centered at l_0. The crystal size distribution is defined based on solvent mass m_W in the crystallizer (i.e., $n(t, l)$ represents the number of crystals at time t with size l per unit mass of solvent in the crystallizer). For the chemical process example under consideration, the initial PSD was that used in Ref. 39:
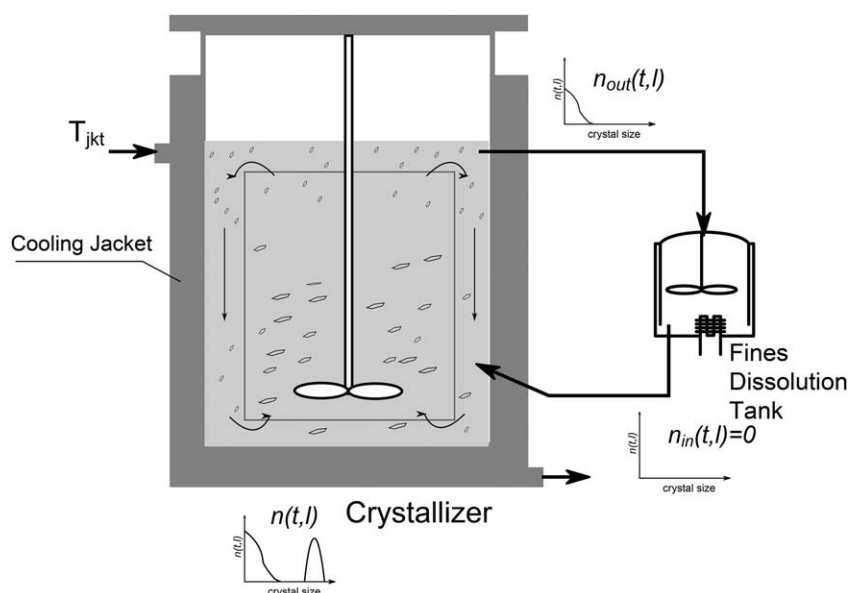

Figure 4. Batch crystallizer with fines dissolution loop scheme.

To illustrate the typical particle-size distributions for the various streams in the crystallizer, example distributions are shown for the solution in the crystallizer (showing a large number of particles at the larger crystal sizes as desired), stream entering the fines dissolution tank (showing that primarily small particles make it through the fines trap), and stream exiting the fines dissolution tank (showing that all crystals have been dissolved).

$$n(t_0, l) = \begin{cases} a_0 (3 \cdot 10^{-4} - l)(l - 2.12 \cdot 10^{-4}) & \text{if } 2.12 \cdot 10^{-4} \leq l \leq 3 \cdot 10^{-4} \ m \\ 0 & \text{otherwise} \end{cases} \tag{13}$$

where the size distribution $n(t, l)$ is based on mass of solvent and has units of $\#/(\mathrm{kg}_W \cdot \mathrm{m})$, with kg_W standing for kilogram of water. The coefficient a_0 is chosen based on the mass of seeds in the crystallizer.

The term $n \frac{d}{dt} \ln m_W$ in Eq. 12 accounts for possible variation of mass of solvent in the crystallizer during batch operation due to its possible accumulation in the fines dissolution tank,[37] while the last term includes the effect of input and output streams related to the fines dissolution loop. Specifically, $\dot{m}_{W,\text{in}}$ and $\dot{m}_{W,\text{out}}$ represent the mass flow rates of solvent into and out of the crystallizer from the fines dissolution tank, and n_{in} and n_{out} are the particle-size distributions in the streams entering and leaving the crystallizer from the fines dissolution tank.

To track the supersaturation during batch operation, the mass balance on species i (where $i = R, S, W$, corresponding to the desired enantiomer, the undesired enantiomer, and the solvent water, respectively) in the liquid phase in the crystallizer can be written as

$$\frac{dm_i}{dt} = \dot{m}_{\text{cryst},i} + w_{\text{in},i} \rho_l \dot{V}_{l,\text{in}} - w_{\text{out},i} \rho_l \dot{V}_{l,\text{out}} \tag{14}$$

In this equation, $\dot{m}_{\text{cryst},i}$ represents the rate (mass/time) at which component i is crystallized (enters the solid phase), and thus it is zero for $i = S$ and $i = W$, but for the desired enantiomer R it is given by

$$\dot{m}_{\text{cryst},R} = -3 m_W \rho_c k_V \int_0^\infty l^2 G n(t, l) dl \tag{15}$$

where ρ_c is the crystal density, ρ_l is the liquid density and k_V is the crystal shape factor (the derivation of this equation is discussed in Part D of the Supporting Information). Moreover, in Eq. 14, the mass fraction of species i in the liquid phase in the inlet stream to the crystallizer ($w_{\text{in},i}$) is equal to the mass fraction of species i in the liquid phase in the fines dissolution tank, and the mass fraction of species i in the liquid phase in the stream out of the crystallizer ($w_{\text{out},i}$) is the same as the mass fraction of species i in the liquid phase in the crystallizer. $\dot{V}_{l,\text{in}}$ and $\dot{V}_{l,\text{out}}$ refer to the liquid volumetric flow rate of the inlet and outlet streams of the crystallizer, respectively.

The energy balance in the crystallizer was taken to be

$$M_{tot} c_p \frac{dT}{dt} = -UA(T - T_{jkt}) \tag{16}$$

where M_{tot} is the total mass in the crystallizer (assumed to be constant), c_p is the heat capacity of the suspension in the crystallizer (assumed to be a constant), T is the temperature of the suspension in the crystallizer, U is the overall heat-transfer coefficient of the crystallizer surface in contact with the jacket, A is the heat exchange area, and T_{jkt} is the jacket temperature. It is noted that the energy balance only accounts for temperature changes in the crystallizer due to the jacket; any heating/ cooling effects due to the streams entering and leaving the fines dissolution tank were considered to be negligible because it was considered that there is perfect temperature control of the stream returning to the crystallizer from the fines

dissolution tank such that the energy flows out of and into the crystallizer are equal and opposite at all times and thus do not contribute to the energy balance.[33] In addition, it was assumed that the time required for heating of the crystals was shorter than the time required for heating of the liquid such that the temperature of the crystals was assumed to be equal to that of the liquid at all times, and the enthalpy of crystallization was assumed to be negligible.

In this work, the contents of the dissolution tank were assumed to be perfectly mixed and to consist only of liquid (i.e., it is assumed that all crystals are dissolved into the mother liquor when they enter the fines dissolution tank so that $n_{\text{in}} = 0$ in Eq. 12). Thus, the mass balance for each component i in the fines dissolution tank is

$$\frac{dm_{\text{diss},i}}{dt} = \dot{m}_{\text{diss},i} + w_{\text{out},i} \rho_l \dot{V}_{l,\text{out}} - w_{\text{in},i} \rho_l \dot{V}_{l,\text{in}} \tag{17}$$

where $m_{\text{diss},i}$ is the mass of species i in the fines dissolution tank, and $\dot{m}_{\text{diss},i}$ represents the rate at which crystal mass is dissolved to liquid mass. Thus, $\dot{m}_{\text{diss},i} = 0$ for $i = S, W$ and $\dot{m}_{\text{diss},R}$ is the rate at which fines crystal mass leaves the crystallizer. If C_{fines} is the fines concentration (in mass of fines crystals per mass of solvent) in the removal stream, the rate of dissolved crystals of R can be given by $C_{\text{fines}} \dot{m}_{W,\text{out}}$. The fines concentration can be calculated with the following equation

$$C_{\text{fines}} = k_V \rho_c \int_0^\infty n_{\text{out}}(t, l) l^3 dl \tag{18}$$

The volumetric flow rate of the fines removal stream ($\dot{V}_{sp,\text{out}}$) is taken to be a constant operational parameter. To keep a constant mass in the crystallizer, the volumetric flow rate ($\dot{V}_{sp,in}$) for the returning stream is given by

$$\dot{V}_{sp,\text{in}} = \dot{V}_{sp,\text{out}} + C_{\text{fines}} \dot{m}_{W,\text{out}} \left(\frac{1}{\rho_l} - \frac{1}{\rho_c} \right) \tag{19}$$

It is noted that if the removal stream is sufficiently diluted, the approximation $\dot{V}_{sp,\text{in}} = \dot{V}_{sp,\text{out}}$ is valid. With Eq. 18 it is possible to get the liquid volumetric flow rate appearing in the mass balances: $\dot{V}_{l,\text{out}} = \dot{V}_{sp,\text{out}} - \dot{m}_{W,\text{out}} \frac{C_{\text{fines}}}{\rho_c}$. Also, as all fines are dissolved, $\dot{V}_{l,in} = \dot{V}_{sp,\text{in}}$.

The fines dissolution tank receives a stream from the crystallizer that is enriched in fines crystals. This enrichment is modeled by setting the crystal number density of the stream leaving the crystallizer to $n_{\text{out}} = h(l) n(t, l)$, where $h(l)$ is calculated from the following equation[40]

$$h(l) = n_{\max} \exp \left[-\left(\frac{l}{2\sigma_l} \right)^2 \right] \tag{20}$$

with $n_{\max} = 0.6$ and $\sigma_l = 0.15$.

To numerically simulate the process described by Eqs. 12–20, a numerical method capable of capturing the features of interest of the particle-size distribution must be chosen. In the crystallization literature, it is common to apply the method of moments to transform the population balance equation into a system of first-order ordinary differential equations that

describe the variations in the moments of the particle-size distribution in time. When the flow to the fines dissolution tank is halted (i.e., $\dot{m}_{W,\text{in}}=\dot{m}_{W,\text{out}}=0$ in Eq. 12), the method of moments can be readily applied to simulate the resulting population balance model, with the j-th order moment of the distribution defined by Eq. 21 ($j=0, 1, \ldots$), and the derivatives of the moments described in Eq. 22.[37]

$$\mu_j=\int_0^\infty l^j n(t,l)dl \qquad (21)$$

$$\frac{d\mu_j}{dt}=\begin{cases} B_0 & \text{if } j=0 \\ \int_0^\infty nGjl^{j-1}dl+l_0^j B_0 & \text{if } j>0 \end{cases} \qquad (22)$$

with $l_0=0$ m in Eq. 22.

However, because the integration required to define the moments removes the dependence of the particle-size distribution characteristics on the characteristic size l by integrating over all particle sizes, the method of moments cannot be applied to numerically simulate the population balance of Eq. 12 when the fines dissolution process is used. This is because the ability of the fines trap to separate larger and smaller crystals is modeled using the function $h(l)$ (Eq. 20) which has an explicit dependence on the particle length, and a numerical method that removes the dependence of the particle-size distribution characteristics on the characteristic length of the particles would be unsuitable for representing the batch crystallization process with fines dissolution described above. Instead, the moving sectional method, to be described in the next section, is utilized to simulate the particle-size distribution of the crystallization process with fines dissolution throughout the batch simulation.

Moving sectional method for crystal nucleation and growth

The moving sectional method[41] (with only nucleation and growth mechanisms of crystal variation) considers the PSD to be divided into M contiguous sections (bins) with lower and upper boundaries given by l_i and l_{i+1} and with the number of particles per mass of solvent in each bin i defined as

$$N_i=\int_{l_i}^{l_{i+1}} n(t,l)dl \qquad (23)$$

It considers that l_i and l_{i+1}, as well as the pivot for each bin (p_i, which is a representative size for the i–th bin) change with time according to the crystal growth rate. After discretization and derivation based on the method of characteristics, the population balance equation (Eq. 12) is expressed for each bin as

$$\frac{dN_i(t)}{dt}=\begin{cases} B_0(t)-N_i\dfrac{d}{dt}\ln m_W+\mathcal{Q}_{I/O,i}(t) & \text{if } i=1 \\ -N_i\dfrac{d}{dt}\ln m_W+\mathcal{Q}_{I/O,i}(t) & \text{if } i=2,\ldots,M \end{cases} \qquad (24a)$$

$$\frac{dp_i}{dt}=\begin{cases} \dfrac{1}{2}\left(\dfrac{dl_1}{dt}+\dfrac{dl_2}{dt}\right) & \text{if } i=1, \\ G(t) & \text{if } i=2,\ldots,M \end{cases} \qquad (24b)$$

$$\mathcal{Q}_{I/O,i}(t)=\frac{1}{m_W}\left[N_{i,in}(t)\dot{m}_{W,\text{in}}-N_{i,out}(t)\dot{m}_{W,\text{out}}\right] \qquad (24c)$$

where $N_{i,\text{in}}(t)\equiv 0$ (because $n_{\text{in}}\equiv 0$) and $N_{i,\text{out}}$ are the number of particles per mass of solvent in each bin i for the input and output streams. Additionally, except for $i=1$, $\frac{dl_i}{dt}=G(t)$ for $i=2,\ldots,M+1$ ($\frac{dl_1}{dt}=0$). The discretization of n_{out} for the i-th bin was taken to be $N_{i,\text{out}}=h(p_i)N_i$, where $h(p_i)$ is given by Eq. 26. The particle-size distribution can be approximated from the states in Eq. 24 using the expression for the i-th bin shown by Eq. 27

$$N_{i,\text{out}}(t)=h(p_i)N_i \qquad (25)$$

$$h(p_i):=n_{\max}\ \exp\left[-\left(\frac{p_i}{2\sigma_l}\right)^2\right] \qquad (26)$$

$$n(t,p_i)=\frac{N_i}{l_{i+1}-l_i} \qquad (27)$$

In this discretization scheme, the bin boundaries l_i at the initial time can be spaced in a size range that covers the entire initial PSD. The pivots p_i at the initial time are defined at the centers of each bin (i.e., $p_i=\frac{1}{2}(l_i+l_{i+1})$). The number of particles per bin N_i is obtained by the integral defined by Eq. 23 using the initial PSD (Eq. 13).

To model growth of the smallest crystals, their corresponding pivots (Eq. 24b) increase with time, with the result that the smallest crystals become characterized by larger average sizes. As particles are nucleated, they must be added to a specific bin, but as the pivots increase, it can happen that the smallest pivot becomes significantly larger than the size at which particles nucleate such that nucleation can no longer be represented properly. The growth of the bins and pivots is also problematic for the selection behavior of the fines trap because it causes the particle-size distribution to lack the number of bins required at lower particle sizes that are required to achieve the desired separation behavior described by $h(l)$ (Eq. 20).

To overcome these difficulties, Ref. 41 proposed that new bins are added to Eq. 24 at intervals separated by time length Δt_{bin} sufficiently small to track the nucleation dynamics and to simulate the fines trap with adequate resolution. Each new bin is added at the minimum crystal size (zero in this work; thus, $p_1=l_1=l_2=0$ at each bin addition). Also, it is considered that each new bin contains no crystals when it is initialized ($N_1=0$ at each bin addition). An efficient numerical scheme of the moving sectional method was implemented for the bin additions that utilizes a constant Δt_{bin} during the simulation for adding new bins. This strategy takes advantage of the fact that once the bins are added in constant intervals Δt_{bin} at the intermediate time steps (not including the initial and final times), at the end of the simulation the total number of bins will be $M_f=M_0+N_t-2$, where N_t can be obtained from the initial and final times as $N_t=\lfloor\frac{t_f-t_0}{\Delta t_{bin}}+0.5\rfloor+1$, where $\lfloor x\rfloor$ signifies the largest integer less than x. Thus, an augmented state sequence $\tilde{y}$ capable of accommodating all the states at the final time can be created before starting the numerical integration, which avoids the need to create new states and renumber the older bins when a new bin is added. Hence, the total number of elements in the sequence $\tilde{y}$ will be $v_{\tilde{y}}=2M_f+v_{\bar{y}}$, where $v_{\bar{y}}$ is the number of elements in the state sequence $\bar{y}$ that contains the extra states required to close the dynamic system, which in this case are the mass of each component in the crystallizer and fines dissolution tank and the crystallizer temperature. N_i and p_i must be integrated for each bin. Further details on the implementation of the moving sectional method in this work are provided in Part E of the Supporting Information.

In this work, the derivatives for the optimization schemes were obtained using automatic differentiation methods, which

involves a substantial amount of data to calculate the derivatives.[42] Thus, it is desired to minimize the computer memory usage for the function evaluations. At each simulation time step, the dynamic system was integrated using a low memory Runge-Kutta method. The two storages register third-order Runge-Kutta method defined by Ref. 43 was chosen, which used derivations from Ref. 44.

Though the moving sectional method involves the calculation of an approximation of the particle-size distribution in time, instead of the moments of the distribution as would be undertaken if the method of moments were used, the moments of the particle-size distribution can be obtained from the moving sectional method as follows

$$\mu_j = \sum_{i=1}^{M} \left[N_i p_i^j \right], j=0, 1, \ldots \qquad (28)$$

Parameter estimation

Obtaining crystal nucleation and growth rates is considered to be a challenging task because of the difficulty of measuring particle sizes and their distributions, especially for small crystal sizes. Even when crystal data is available that can be used for estimating the parameters of nucleation and growth rate models, the experimental conditions under which that data was obtained may be different from the conditions for which a nucleation and growth rate model is desirable (one approach to deal with this issue is the use of Kinetic Monte Carlo simulation[45]) In the particular case of mandelic acid, an additional difficulty for determining crystal nucleation and growth rates is that the presence of the opposite enantiomer in the mother liquor can affect the nucleation and growth kinetics of the desired enantiomer.[39]

There are few studies in the literature addressing the estimation of kinetic parameters for enantiomeric system crystallization. For example, for the R-MA case, Ref. 12 studies the unseeded cooling batch crystallizer to evaluate the growth and nucleation. A growth-only kinetics evaluation of S-mandelic acid and the opposite enantiomer effects were investigated by Ref. 46.

Reference 39 experimentally evaluates the direct crystallization of a partially resolved system of R-MA enantiomer in water solution during batch operation (on lab-scale and without fines dissolution). They study the influence of various operating condition changes and the presence of the opposite enantiomer (S-MA) on the nucleation and growth of R-MA. They propose the use of the nucleation rate model $B_0 = k_{b0} \exp\left(-\frac{E_b}{R_g T}\right) \Delta c_R^b M_T$ and the growth rate model $G = k_{g0} \exp\left(-\frac{E_g}{R_g T}\right) \Delta c_R^g$, where $b, k_{b0}, E_b, g, k_{g0}$, and E_g are model parameters, R_g is the gas constant, and M_T is the suspension density (ratio of crystal mass to solvent mass). The term $\Delta c_R := c_R - x_R c_{sol}^{eq}$, where c_R is the R-MA concentration (g R-MA/g of water) and x_R is given by $\frac{c_R}{c_R + c_S}$, represents the supersaturation of R in the presence of the S enantiomer with concentration c_S. The term c_{sol}^{eq} is the solubility of the mixture solution, which is given by a fitted polynomial function of both temperature and composition. To estimate the parameters k_{b0}, E_b, k_{g0} and E_g, data was gathered from batch crystallization experiments performed for controlled linear cooling with different operating conditions. Then, a constrained least-squares estimation was performed to determine the model parameters by minimizing the difference between the measurements of the R-MA concentration in the system (g R-MA/g of water) and the values of the R-MA

Table 2. Operating Parameters Used for Parameter Estimation (Run 2 from[39])

Parameter	Notation	Value	Unit
Initial temperature	$T(t_0)$	23.0	°C
Final temperature	$T(t_f)$	19.0	°C
Batch time	t_f	200.0	min
Solvent mass	m_W	200.0	g
Initial R liquid mass	$m_R(t_0)$	0.0275	kg
Initial purity	P^i	0.82	(-)
Seed mass	$m_c(t_0)$	0.34	g
Initial zero moment	$\mu_0(t_0)$	$6.110 \cdot 10^5$	#/kg$_W$
Initial first moment	$\mu_1(t_0)$	156.4296	m/kg$_W$
Initial second moment	$\mu_2(t_0)$	0.04028	m²/kg$_W$
Initial third moment	$\mu_3(t_0)$	$1.0435 \cdot 10^{-5}$	m³/kg$_W$
Initial fourth moment	$\mu_4(t_0)$	$2.7184 \cdot 10^{-9}$	m⁴/kg$_W$
R crystal density	ρ_c	1349.0	kg/m³
Crystal shape factor	k_V	0.12	(-)
Eutectic purity	P^e	0.69	(-)
Kinetic nucleation order	b	1.5	(-)
Kinetic growth order	g	1.0	(-)
Seed coefficient	a_0	$5.38 \cdot 10^{18}$	#/(kg$_W \cdot$ m³)

concentration calculated based on population balance equations with the growth and nucleation rate expressions.

In this work, we use crystal nucleation and growth rate expressions similar to those from Ref. 39 but replacing the term Δc_R with the term $(S_{sup}-1)$,[47] where S_{sup} is the supersaturation defined with respect to the solubility of R in the liquid phase. This expression for supersaturation, where $S_{sup} = \frac{w_R}{w_{R,sat}}$, is consistent with the literature[19] and eliminates the need for the experimentally developed fit for the solubility data utilized by Ref. 39 and instead allows for use of solubility data derived from the ternary diagram in determining the crystal growth and nucleation rates. Specifically, using w_R^{sat} computed from Eq. 3, we use the following expressions for the nucleation and growth rates

$$B_0 = k_{b0} \, \exp\left(-\frac{E_b}{R_g T}\right) (S_{sup}-1)^b M_T \qquad (29)$$

$$G = k_{g0} \, \exp\left(-\frac{E_g}{R_g T}\right) (S_{sup}-1)^g \qquad (30)$$

Because of the difference between the growth rate expressions used in this work and those determined by Ref. 39, we estimate the parameters of the nucleation and growth rate expressions in Eqs. 29–30 using the data available in Ref. 39 (run 2) with the operating conditions listed in Table 2.

For consistency with Ref. 39 the parameter estimation is performed for batch operation without fines dissolution by determining the values of the growth rate parameters that minimize a constrained least-squares problem that penalizes in the objective function the difference between calculated and experimental values of the concentration of the R enantiomer in the crystallizer. The moment equations (Eq. 22) were used to calculate the values of the R concentration used in the least-squares estimation. The first five moment equations were used to capture the dominant dynamics of the system,[48] along with a mass balance on R, as follows

$$\frac{dm_R}{dt} = -3 m_W \rho_c k_V \mu_2 G(t) \qquad (31a)$$

$$\frac{d\mu_j}{dt} = \begin{cases} B_0, \, j=0 \\ jG(t)\mu_{j-1}, \, j=1, 2, 3, 4 \end{cases} \qquad (31b)$$

where B_0 and $G(t)$ are defined in Eqs. 29 and 30, and $m_R(t)$ represents the mass of enantiomer R in the liquid phase in the

crystallizer at time t. The initial moments (reported in Table 2) were obtained using the initial PSD (Eq. 13) and the definition in Eq. 21. The seed mass is calculated based on the third order moment as: $m_c(t_0) = m_W \rho_c k_V \mu_3(t_0)$. No energy balance was required in this simulation for consistency with Ref. 39, which assumed that the temperature in the crystallizer followed a linear cooling profile from 23°C to 19°C. During the simulation, the crystal yield can be obtained using: $Y_c = \frac{m_c(t_f) - m_c(t_0)}{m_R(t_0)}$, in which $m_c(t)$ is the mass of crystals at time t and is given by $m_c(t) = m_W \rho_c k_V \mu_3(t)$, where t_f is defined as the final time and t_0 as the initial time of the batch. Moreover, as the crystallization process without a fines dissolution loop is a closed system, all the formed crystal mass is from the liquid phase (i.e., $m_c(t_f) - m_c(t_0) = m_R(t_0) - m_R(t_f)$), such that the yield can be written as: $Y_c = 1.0 - \frac{m_R(t_f)}{m_R(t_0)}$.

As suggested by Ref. 39, the parameters $k_{b0}, E_b, k_{g0},$ and E_g were estimated using a least-squares minimization between the predicted (i.e., from Eqs. 29–31) and experimental values of the concentration of R in the liquid phase throughout the batch. In the predictions, the coefficients b and g in the growth and nucleation rate expressions were set to 1.5 and 1.0, respectively, for consistency with Ref. 39. Also for consistency with Ref. 39, a constraint on the ratio $L_{43} = \frac{\mu_4}{\mu_3}$ (volume-weighted mean size) at the end of the batch was included to account for experimental results on the size distribution. An additional constraint was added for the present work on the process yield to take advantage of additional information reported in Ref. 39 for the experimental crystal yield (Y_c).

The parameter estimation problem with $\theta = [k_{b0}, k_{g0}, E_b, E_g]$ is stated as:

$$\underset{\theta}{\text{minimize}} \quad J(\theta) = \sum_{i=1}^{n_t} \left[c_R(t_i)^{\text{exp}} - c_R(t_i)^{\text{calc}} \right]^2$$

$$\text{subject to} \quad 0.9 L_{43}^{\text{exp}} \leq \frac{\mu_4}{\mu_3} \leq 1.1 L_{43}^{\text{exp}}$$

$$0.95 Y_c^{\text{exp}} \leq \left[1.0 - \frac{m_R(t_f)}{m_R(t_0)} \right] \leq 1.05 Y_c^{\text{exp}}$$

$$(32)$$

The calculated concentration of R at time t_i, $c_R(t_i)^{\text{calc}}$, is given by $\frac{m_R(t_i)}{m_W}$ based on Eqs. 29–31, with the temperature set to the linear cooling strategy for run 2 in Ref. 39 (i.e., perfect temperature control was assumed, and Eq. 16 was not solved), $c_R(t_i)^{\text{exp}}$ is the experimental concentration at time t_i and n_t is the number of experimental samples used (50 data points, which were extracted from the plots for run 2 in Ref. 39) The experimental values of the mean size and yield used were $L_{43}^{\text{exp}} = 440.1$ μm and $Y_c^{\text{exp}} = 8.5\%$, respectively, as reported Ref. 39 for run 2. The parameter estimation problem in Eq. 32 was solved using IPOPT[49] and ADOL-C[42] for the gradient and Jacobian. The dynamic model of Eq. 31 was solved using the Explicit Euler numerical integration method with an integration step size of 1 s.

The parameter estimation problem of Eq. 32 resulted in the following estimated parameter values: $k_{b0} = 1.6416 \cdot 10^{12}$ $\frac{\#}{\text{kg}_W \text{s}}$, $k_{g0} = 54416.74$ $\frac{\text{m}}{\text{s}}$, $E_b = 33297.23$ $\frac{\text{J}}{\text{mol}}$ and $E_g = 63862.05$ $\frac{\text{J}}{\text{mol}}$. The upper bounds for the L_{43} and Y_c constraints were active for this solution. Figure 5 shows the comparison between the experimental (EXP-ZR in Figure 5) concentrations and calculated concentrations from the moment model (MOM in
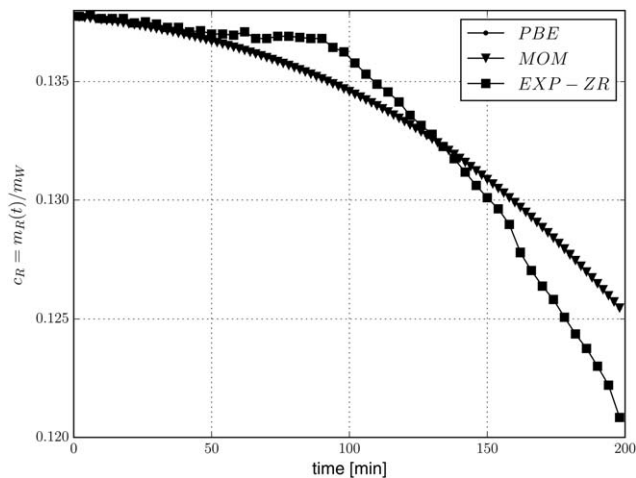

Figure 5. Experimental and calculated concentration profiles for parameter estimation based on Table 2.

PBE: simulation with moving sectional method (Eq. 24); MOM: method of moments simulation (Eq. 31; overlays PBE); EXP-ZR is the experimental data extracted from Ref. 39

Figure 5) using these estimated parameter values. To verify the adequacy of the moment model of Eq. 31b for numerically simulating the crystallization process, the moving sectional method of Eq. 24 for the case without a fines dissolution loop ($\dot{m}_{W,\text{in}} = \dot{m}_{W,\text{out}} = 0$) was also used to determine the predictions of the concentration of R in the liquid phase throughout the batch and was plotted for comparison in Figure 5 (labeled PBE in the figure). The trajectories calculated from the moving sectional method and the method of moments overlaid one another, verifying that the first five moments of the particle-size distribution were sufficient for modeling the dominant process dynamics in this case. Although the predicted and experimental values of the concentration profiles show some offset, a number of factors may be responsible for this. First, because in Ref. 39 did not report the exact values of their experimental data points but only plotted the data, there may be some inaccuracy in the experimental values used for the parameter estimation in this work due to the need to extract the values from the plots. In addition, errors may be introduced for the same reasons noted in Ref. 39 as causes for offset between the experimental and predicted R concentrations in their own work, namely limitations of the particle-size measurement equipment and modeling approximations such as neglecting breakage and agglomeration and assuming a narrow seed initial particle-size distribution. However, it is notable that the particle-size distribution obtained by simulating the batch process with linear cooling with the parameter values estimated from Eq. 32 shows many similarities to the predicted particle-size distribution developed for run 2 from Ref. 39. This particle-size distribution is shown in Figure 6, simulated using the moving sectional method with the growth and nucleation rates determined by solving Eq. 32. The evolution of the particle-size distribution throughout the batch is plotted by showing the particle-size distribution at five different times (2, 50, 100, 150, and 198 min) after the batch was initiated.

REMARK 5. *Because the parameter estimation in Eq. 32 is a nonlinear program, the parameters obtained for the*
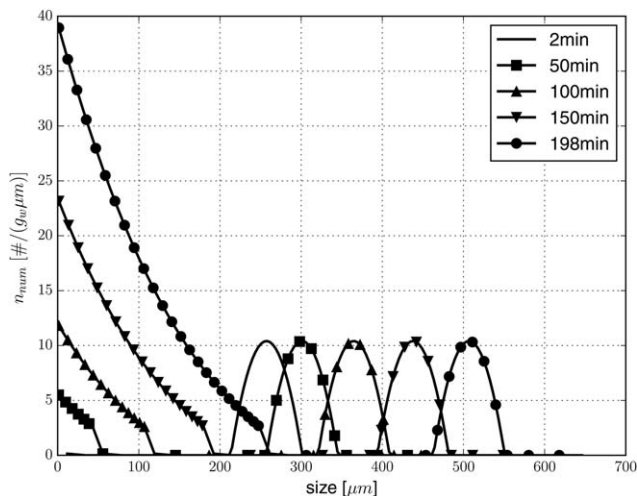
Figure 6. Calculated PSD (using Eq. 27 in number of particles per gram of solvent (g_w) and micrometer) at five times after the batch crystallization process was initiated (crystallization begins at 0 min) without fines dissolution under the linear cooling strategy with the parameters k_{b0}, k_{g0}, E_b, and E_g estimated from Eq. 32.

growth and nucleation rates do not necessarily correspond to a global optimum, but the good agreement of the experimental results with the results from the parameter estimation in Figure 5 *indicates that the results are expected to be sufficient for simulating the growth and nucleation rates.*

Batch Crystallization Study

In the next two sections, we complete the demonstration of the process operation, modeling, and control policy developed in the section "Batch crystallization operation and controller design using ternary diagram data" by demonstrating the application of model predictive control to the batch crystallization process of the section "Batch Crystallizer Model with Fines Dissolution Loop." Specifically, for this mandelic acid in water example, Steps 1–4 of the proposed operation, modeling, and control strategy were demonstrated in the section "Batch crystallization operation and controller design using ternary diagram data," and Step 5 was demonstrated in the section "Batch Crystallizer Model with Fines Dissolution Loop." In the following two sections, we demonstrate Steps 6–8. We investigate the closed-loop performance of the batch crystallization process in both the case without the fines dissolution loop and the case with the fines dissolution loop to demonstrate the applicability of MPC in controlling a batch enantioselective crystallization process for a racemic compound forming system.

Optimal jacket temperature profile without fines dissolution

In this section, the batch crystallization of R-MA enantiomer without the fines dissolution loop is considered. Because the experimental data for crystal nucleation growth kinetics parameter estimation[39] was available only within the temperature range of 23°C to 19°C, an operating temperature range that deviated from this temperature range by only a few degrees above and below was chosen for the batch

crystallization process. Specifically, Figure 2 was analyzed to determine a reasonable operating temperature range, assuming that the initial purity P^i is fixed at 0.80, close to the purity used to obtain the growth and nucleation rate parameters, from the pre-enrichment process, and that it is desired to obtain the greatest yield possible during the crystallization process by crystallizing until the eutectic purity P^e is reached. The top figure in Figure 2 was analyzed, and it was seen that cooling a solution with an initial R mass fraction of 0.1336 would allow a saturated solution at 26.0°C to be cooled to reach the eutectic composition at 12.13°C. Thus, due to its closeness to the 23°C to 19°C operating temperature range from Ref. 39, the 26.0°C to 12.13°C operating temperature range was chosen for this example. Also, the batch process was scaled up compared to Ref. 39 (i.e., a total initial liquid mass of 20 kg was assumed) with $P^i = 0.80$ and seeding with 28.92 g of R to maintain approximately the same ratio of seeds to mass of solvent as in Table 2. Table 3 lists the operational parameters used in this case study. The liquid density and heat capacity are assumed to be close to those of the solvent, and the thermal coefficient is on an order of magnitude consistent with the value in Ref. 35.

A model predictive controller was used to control the batch crystallization process to minimize the ratio of the mass of crystals grown from nuclei to the mass of crystals grown from the seeds. The model developed for use within the MPC tracked the population balance characteristics using the method of moments. To accomplish the control objective of maximizing the mass of crystals obtained from seeds while reducing the mass of crystals obtained from nucleation, the model used two sets of five moment equations, one for crystals growing from seeds and one for crystals growing from nuclei.[35] Applying this scheme, the differential equations for mass, energy and moments for the model used within the MPC are

$$\frac{dm_R}{dt} = -3m_W \rho_c k_V (\mu_2^n + \mu_2^s) G(t) \tag{33a}$$

$$M_{tot} c_p \frac{dT}{dt} = -UA(T - T_{jkt}) \tag{33b}$$

Table 3. Operational Parameters Used in Optimal Control Study Without Fines Trap

Parameter	Notation	Value	Unit
Initial temperature	$T(t_0)$	26.0	$^{\circ}$C
Final temperature	$T(t_f)$	12.13	$^{\circ}$C
Batch time	t_f	30	h
Solvent mass	m_W	16.658	kg
Initial R liquid mass	$m_R(t_0)$	2.673	kg
S liquid mass	m_S	0.668	kg
Initial purity	P^i	0.80	(-)
Seed mass	$m_c(t_0)$	28.92	g
Initial zero moment	$\mu_0(t_0)$	$6.281 \cdot 10^5$	#/kg$_W$
Initial first moment	$\mu_1(t_0)$	160.7909	m/kg$_W$
Initial second moment	$\mu_2(t_0)$	0.04140	m^2/kg$_W$
Initial third moment	$\mu_3(t_0)$	$1.0724 \cdot 10^{-5}$	m^3/kg$_W$
Initial fourth moment	$\mu_4(t_0)$	$2.7935 \cdot 10^{-9}$	m^4/kg$_W$
R Crystal density	ρ_c	1349.0	kg/m^3
Liquid density	ρ_l	1000.0	kg/m^3
Crystal shape factor	k_V	0.12	(-)
Seed coefficient	a_0	$5.53 \cdot 10^{18}$	#/(kg$_W \cdot$ m^3)
Thermal coefficient	UA	250	W/K
Heat capacity	c_p	$3.8 \cdot 10^3$	J/(K $\cdot$ kg)

$$\frac{d\mu_0^\nu}{dt} = B_0^\nu, \ \nu = n, s \tag{33c}$$

$$\frac{d\mu_j^\nu}{dt} = jG(t)\mu_{j-1}^\nu, \ j=1,2,3,4, \ \nu = n,s \tag{33d}$$

where ν designates the seeds (s) or nucleation (n) moments. No breakage or agglomeration is considered, and $B_0^s = 0$. The growth rate $G(t)$ is given by Eq. 30 and B_0^n by Eq. 29 with the parameters obtained from Eq. 32. The initial values of μ_j^n, $j=0,1,2,3,4$, are zero. Initial values for m_R, T, and μ_j^s, $j=0,1,2,3,4$, are reported in Table 2.

The MPC optimization problem at each sampling time can be stated as

$$\underset{\Delta T_{jkt,k}}{\text{minimize}} \qquad J(T_{jkt,k}) := \frac{\mu_3^n(t_f)}{\mu_3^s(t_f)} \tag{34a}$$

$$\text{subject to:} \qquad \text{Model : Eq. 33} \tag{34b}$$

$$\Delta T_{jkt,k} \leq 0, k=k_{it}, \ldots, k_{N_t-1} \tag{34c}$$

$$T_{\min} \leq T(t_f) \leq T_{\max} \tag{34d}$$

$$Y_c(t_f) = \frac{P^i - P^e}{P^i(1-P^e)} \tag{34e}$$

in which the decision variables are $\Delta T_{jkt,k} = T_{jkt,k} - T_{jkt,k-1}$, where $k=k_{it}, \ldots, k_{N_t-1}$, with k_{it} at the current sampling time $t_{k_{it}}$ and N_t as the total number of sampling times between t_0 and t_f, and with each value of t_k separated by a sampling period of length Δ. $T(t_k)$ is the temperature within the crystallizer at time t_k. A shrinking prediction horizon was used for the optimization problem that was initially set to $N_t - 1$ and decreased by one at each subsequent sampling time in the simulation so that the remainder of the batch was included in the prediction horizon at all times. The constraint $\Delta T_{jkt,k} \leq 0$ indicates that no heating was allowed (cooling was enforced to enable crystallization). $Y_c(t_f)$ is the crystal yield at the end of the batch, defined by Eq. 8, which is forced to the maximum value 0.4435 obtained by setting $P^f = P^e$ in Eq. 8. No feasibility issues were encountered during the dynamic simulations with this terminal constraint on the yield, indicating that the batch time was sufficiently long to allow this constraint, which essentially requires thermodynamic equilibrium at the end of the batch, to be met. The minimum temperature $T_{\min}$ was set to the temperature required to achieve the eutectic composition ($T_{\min} = 12.13°$C from Eq. 10). For consistency with standard MPC formulations, a maximum temperature $T_{\max} = 30°$C was also included, although due to the cooling constraint of Eq. 34c, it was never approached. The sampling period Δ was set to 360 s and the ordinary differential equations (Eq. 33) were solved using the low memory Runge-Kutta scheme RK33 from Ref. 43. The gradient of the objective function and Jacobian of the constraints were obtained using ADOL-C. The optimization problem was solved with the interior point optimization software package IPOPT.

To simulate the closed-loop crystallization process, Eq. 12 (with $\dot{m}_{W,\text{in}} = \dot{m}_{W,\text{out}} = 0$) was discretized and solved using the moving sectional method (Eq. 24).[41] A new bin was added every sampling time ($\Delta t_{\text{bin}} = \Delta = 360$ s). Thus, at the initial time there are $M_0 = 50$ active bins, so at the final time the number of active bins is $M_f = M_0 + N_t - 2$ (bins added only at the intermediate steps, that is, not at the initial or final times). The $(M_f - M_0)$ bins initially are considered to contain zero crystals and are activated according to the methodology described in the section "Moving sectional
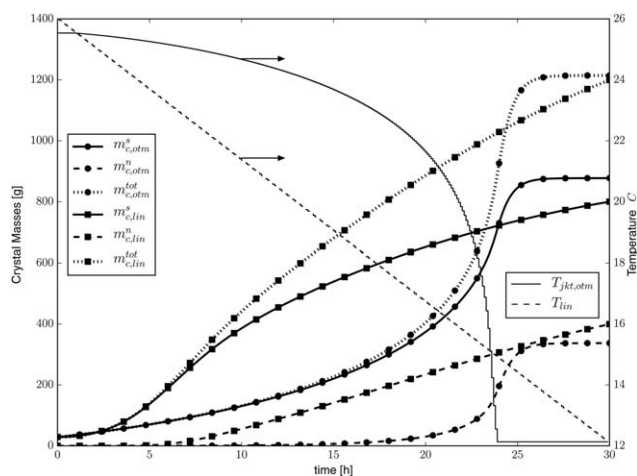

Figure 7. Crystal mass using linear cooling (*lin*) and optimized profile under MPC (otm) in batch crystallization.

The optimized case has jacket temperature $T_{jkt,\text{otm}}$, crystal mass from seeds $m_{c,\text{otm}}^s$, nuclei mass $m_{c,\text{otm}}^n$ and total crystal mass $m_{c,\text{otm}}^{\text{tot}}$. The linear cooling case has crystallizer temperature T_{lin}, crystal mass from seeds $m_{c,\text{lin}}^s$, nuclei mass $m_{c,\text{lin}}^n$ and total crystal mass $m_{c,\text{lin}}^{\text{tot}}$. The two arrows pointing to the right indicate that the y axis for the temperature trajectories is on the right of the plot, whereas it is on the left for the mass profiles.

method for crystal nucleation and growth" and Part E of the Supporting Information.

To enable feedback to the MPC when the plant dynamics are assumed to follow Eqs. 33a,b and the population balance equation is solved using the moving sectional method, the values of m_R, T, and also of the moments of the particle-size distribution must be measured and fed back to the MPC at each sampling time so that the model of Eq. 34b can be integrated at the new sampling time. The values of m_R and T can be obtained in a straightforward manner from numerical integration of Eqs. 33a,b. The moments μ_j^s, $j=0,1,2,3,4$ can be obtained from the last M_0 bins while the moments μ_j^n, $j=0,1,2,3,4$, can be obtained from the first $M_f - M_0$ bins at a given time when the moving sectional method is used with bin additions, as follows

$$\mu_j^s = \sum_{i=M_f-M_0+1}^{M_f} \left[N_i p_i^j\right], j=0,1,2,3,4 \tag{35a}$$

$$\mu_j^n = \sum_{i=1}^{M_f-M_0} \left[N_i p_i^j\right], j=0,1,2,3,4. \tag{35b}$$

The closed-loop simulation results for the batch crystallization process without fines dissolution under the model predictive control strategy of Eq. 34 are shown in Figure 7. These closed-loop profiles under MPC are compared with the closed-loop trajectories under the linear cooling strategy from 26 to 12.13°C during the 30 h operation. Specifically, the dynamic behavior of the mass of crystals from the seeds and the mass of crystals from nucleation are compared for the closed-loop crystallizer under MPC and under the linear cooling strategy. Figure 7 shows that the crystal mass from the seeds is 9.65% greater for the process operated under the MPC than under the linear cooling strategy, and there is also less total crystal mass due to nucleation. On the same plot, the jacket profile

computed by the MPC of Eq. 34 is shown ($T_{jkt,\text{otm}}$ in Figure 7), and the temperature in the crystallizer when a linear cooling profile from $26°$C to $12.13°$C is used (denoted by T_{lin} in the figure) is shown. The flattening of the jacket temperature profile occurs under the control actions calculated by the MPC to optimize the objective function subject to the constraints in the MPC. Because the yield constraint essentially requires that thermodynamic equilibrium be reached at the end of the batch, it is reasonable to expect that the jacket temperature will need to remain constant at the eutectic temperature for some time at the end of the batch to allow thermodynamic equilibrium to be reached.

Under MPC, the temperature is slowly decreased at the beginning of the batch to suppress nucleation, which is consistent with previous studies on batch crystallization.[36,50] As the order of dependence of nucleation rate on supersaturation is greater than the order of dependence of the growth rate on supersaturation ($b > g$), the optimal profile induces a small supersaturation magnitude during most of the operation. However, at approximately 24 h of operation there is a supersaturation peak that quickly enhances the crystal growth and leads to a burst of new crystals. The supersaturation peak timing is optimized in a way to maintain a relatively low rate of solute mass transfer to the new generated crystals.[50] This behavior is shown in Figure 8, which compares the supersaturation profile for the optimized operation ($S_{\text{sup,otm}}$) and the linear run ($S_{\text{sup,lin}}$).

Figure 9 depicts the mass fraction trajectory in the ternary diagram during the batch crystallization. At the initial time the solution in the crystallizer has a composition represented by point **P** and, as it is being cooled, the R enantiomer in the liquid phase is crystallizing. Because of the yield constraint in Eq. 34e, the solution in the crystallizer is forced to achieve the eutectic purity P^e at the final time. Note that the nonequilibrium points were used in the ternary diagram to allow a visualization of the process with respect to the solid–liquid equilibrium.

Figure 10 shows the particle-size distribution at the end of the batch for the process under both MPC and the linear cooling strategy. The bottom plot shows that the optimal policy was able to produce larger crystals originated from the seeds by the final time. The linear cooling approach gives a lower total number of crystals at the final time than the MPC approach (although the total mass of the crystals from nuclei is less for
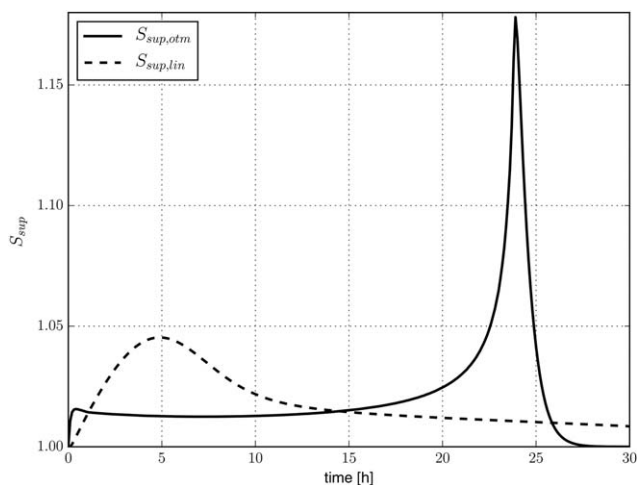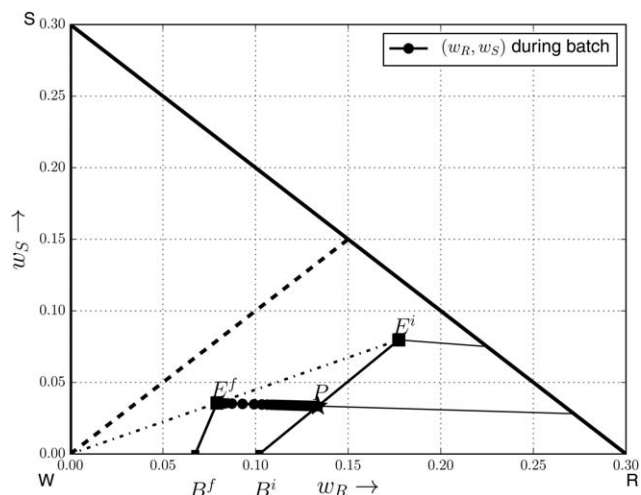

Figure 9. Batch crystallization trajectory in the ternary diagram starting at point P and ending at the eutectic composition E^f.

Each • represents the composition of the liquid in the crystallizer, with 24 min time intervals between successive points. Note that the diagram was zoomed in around the solvent corner for a better visualization. The dashed line with a slope of 1 represents the racemic composition. The dashed-dotted line through E^f and E^i represents a line of constant eutectic purity. The bold line with a slope of -1 in this figure represents a line of constant solvent composition $w_W = 0.7$ (only the portion of the ternary diagram to the right of this line is plotted in the figure).

the MPC approach than the linear cooling approach). This is due to the way the MPC objective function was formulated (Eq. 34a), as it seeks to minimize the mass of fines crystals compared to the mass from seeds, instead of the number. This fact motivates the investigation of including the fines dissolution loop, which will be discussed in the next section.

As noted in the section "Batch crystallization operation and controller design using ternary diagram data," the MPC of Eq. 34 will compute different control actions for different t_f because the objective function (Eq. 34a) and the constraints (Eqs. 34d, e) depend on the final batch time. Thus, as in Step 7 of the operation, modeling, and control procedure developed in the section "Batch crystallization operation and controller design using ternary diagram data," closed-loop simulations of the crystallization process with different final batch times can be evaluated to determine the desired final batch time. To investigate this for the batch crystallization process without fines dissolution under the MPC of Eq. 34, closed-loop simulations were performed with t_f ranging from 20 h to 130 h in 5 h increments. The mass of crystals from nuclei and seeds at the end of each batch is plotted in Figure 11. This figure shows that there is a trade-off between maximizing the crystal mass from seeds and reducing the final batch time (i.e., increases in final batch time correspond to production of more crystals from seeds and less from nuclei), which is because increasing the batch time allows the system to operate with a lower cooling rate, and thus a smaller supersaturation. This plot can be used to understand the tradeoff and choose a batch time with a reasonable length that gives reasonably high production of crystals from seeds. Alternatively, if none of the combinations of batch time with crystal production from seeds is acceptable, another operating strategy can be proposed for the batch crystallization process. One strategy for enhancing the crystal mass formed from

Figure 8. Supersaturation profiles for linear cooling (lin) and optimized operation under MPC (otm).
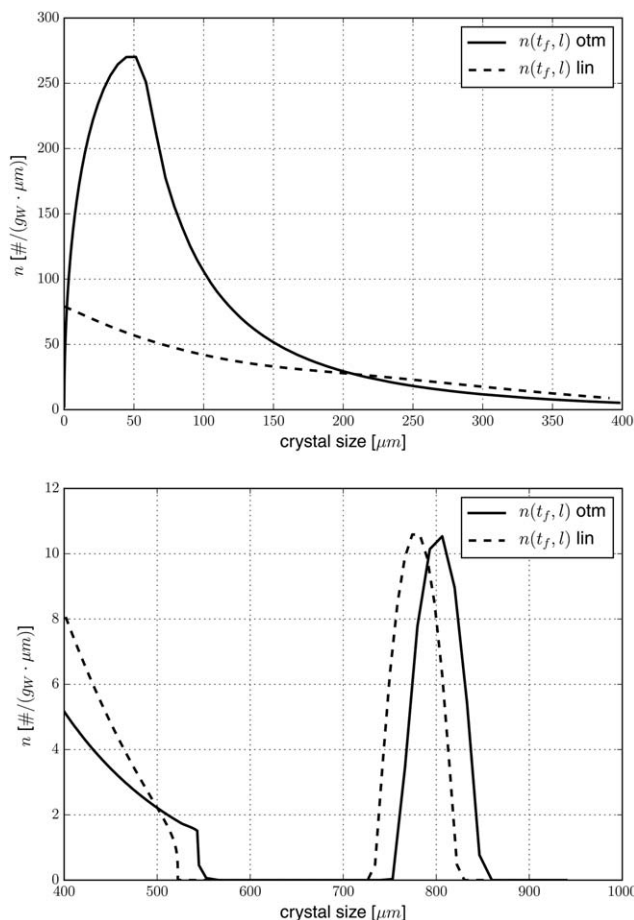
Figure 10. PSD at the end of the batch crystallization process without a fines dissolution loop for linear (lin) and optimal (otm) jacket temperature profiles.

Top: PSD for 0 to 400 µm and Bottom: 400 to 1000 µm. The plots have independent x and y scales.

seeds and hence attenuating long batch times is the use of a fines dissolution loop.[36] Thus, in the following the operation of the batch crystallization process with the fines dissolution scheme is evaluated.
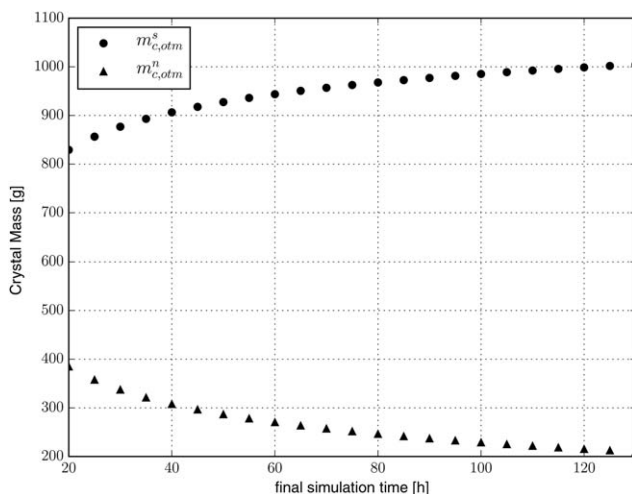

Figure 11. Optimal crystal mass from seeds $m_{c,otm}^s$ and nucleation $m_{c,otm}^n$ using different batch final times.

Table 4. Operational Parameters Used in Optimal Control Study with Fines Trap

Parameter	Notation	Value	Unit
Initial temperature	$T(t_0)$	26.0	°C
Final temperature	$T(t_f)$	12.13	°C
Batch time	t_f	30	h
Crystallizer initial solvent mass	$m_{\mathrm{cryst},W}(t_0)$	13.057	kg
Crystallizer initial R liquid mass	$m_{\mathrm{cryst},R}(t_0)$	2.095	kg
Crystallizer initial S liquid mass	$m_{\mathrm{cryst},S}(t_0)$	0.5237	kg
Dissolver initial solvent mass	$m_{\mathrm{diss},W}(t_0)$	3.601	kg
Dissolver initial R liquid mass	$m_{\mathrm{diss},R}(t_0)$	0.5778	kg
Dissolver initial S liquid mass	$m_{\mathrm{diss},S}(t_0)$	0.1444	kg
Initial purity	P^i	0.80	(-)
Seed mass	$m_c(t_0)$	28.92	g
R crystal density	ρ_c	1349.0	kg/m³
Liquid density	ρ_l	1000.0	kg/m³
Crystal shape factor	k_V	0.12	(-)
Seed coefficient	a_0	$7.0552 \cdot 10^{18}$	#/(kg$_W$ · m³)
Thermal coefficient	UA	250	W/K
Heat capacity	c_P	$3.8 \cdot 10^3$	J/(K·kg)
Dissolver tank total mass	$m_{\mathrm{diss},L}$	4.3236	kg

REMARK 6. *The parameters of the growth and nucleation rate equations were obtained from experiments using a linear cooling strategy. Reference 39 indicates that different cooling rates may impact the growth and nucleation rates. The impact of the nonlinear cooling rate for the crystallizer under MPC on the growth and nucleation rates in the model utilized by the MPC could be analyzed when developing the MPC model for an industrial application.*

Inclusion of fines dissolution loop

To simulate the crystallization process with the fines dissolution loop, the same total liquid mass of each component as in the case without the fines dissolution loop was considered; however, that mass was divided between the crystallizer and the fines dissolution tank. The total mass in the fines dissolution tank was 4.3236 kg, and thus the crystallizer liquid mass was 15.6764 kg (giving the same total liquid mass of 20 kg as in the previous case without the fines dissolution tank). Additionally, the same initial composition was used for each component ($w_R = 0.13364$, $w_S = 0.03341$ and $w_W = 0.83294$) as in the case without the fines trap for both the crystallizer and fines dissolution tank. Using those considerations, the initial masses of all components in the crystallizer and dissolution tank are depicted in Table 4, in addition to other operating parameter values.

To obtain the same initial seed mass in the crystallizer as in the case without fines dissolution, the parameter a_0 in Eq. 13 was adjusted as: $a_0 = a_0^{\mathrm{ref}} \frac{m_W^{\mathrm{ref}}}{m_{\mathrm{cryst},W}}$, in which the superscript *ref* indicates the case without the fines dissolution tank. As there is less mass of solvent in the crystallizer for the case with the fines dissolution tank, $a_0 > a_0^{\mathrm{ref}}$, which means that there are more crystals of each size in the initial PSD for the case with the fines dissolution tank than without it to obtain the same initial seed mass in the crystallizer.

The death function of Eq. 20 can be defined using the pivots as in Eq. 26 and the number of crystals leaving the crystallizer
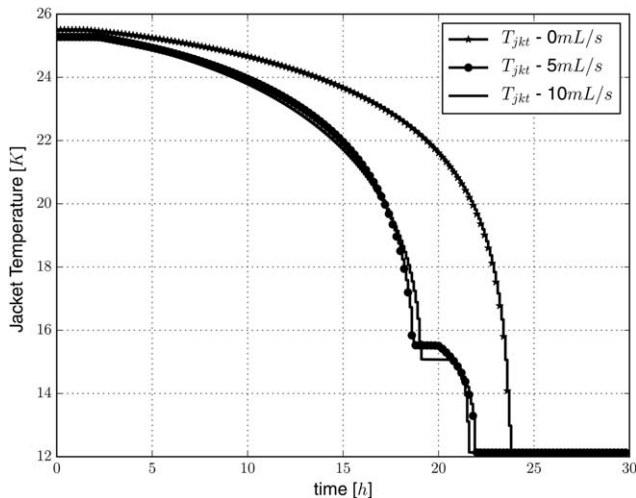
Figure 12. Optimal jacket temperature profiles for $\dot{V}_{sp,\text{out}}$ equal to 0 (starred trajectory), 5 (dotted trajectory) and 10 $\frac{\text{mL}}{\text{s}}$ (solid trajectory).

for each bin ($N_{i,\text{out}}$) was defined by Eq. 25. The fines concentration (Eq. 18) is approximated by $C_{\text{fines}} = k_V \rho_c \sum_{i=1}^{M} \left[N_{i,\text{out}} p_i^3 \right]$. Additionally, the rate of crystallization of the R enantiomer is approximated by $\dot{m}_{\text{cryst},R} = -3\rho_c k_V m_W \sum_{i=1}^{M} \left[N_i p_i^2 G(t) \right]$.

The proposed MPC formulation from Eq. 34 was used, but the controller model was changed to the moving sectional method, instead of the moment model, to include the fines removal effect in the particle-size distribution. The discretized model was solved using the augmented state approach described in the section "Moving sectional method for crystal nucleation and growth" with $M_0 = 30$ and uniformly spaced bins covering the initial PSD for setting the initial number of crystals in each bin and the initial pivots. The same sampling period and final batch time were used as in the section "Optimal jacket temperature profile without fines dissolution." Because of the higher model complexity, a higher
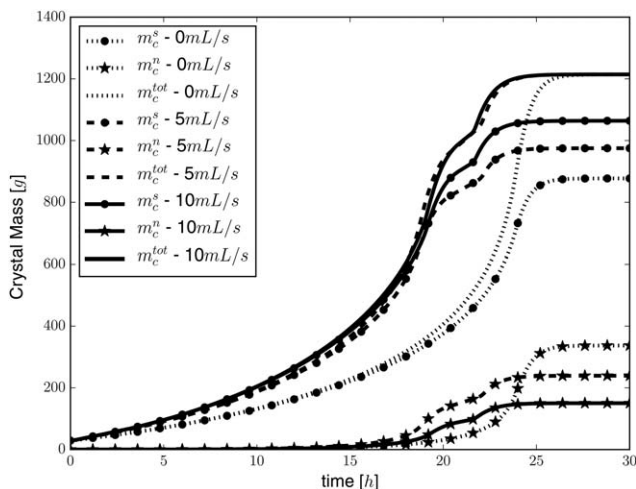

Figure 14. Comparison of crystal number density at final batch time with $\dot{V}_{sp,\text{out}}$ equal to 0, 5, and 10 $\frac{\text{mL}}{\text{s}}$.

Top: PSD for 0 to 400 μm and Bottom: 400 to 1000 μm. The initial PSD for the fines dissolution case is also plotted for comparison. The plots have independent x and y scales.

Figure 13. Crystal masses using $\dot{V}_{sp,\text{out}}$ equal to 0, 5 and 10 $\frac{\text{mL}}{\text{s}}$ and applying optimal jacket temperatures profiles.

In this figure, m_c^s signifies the crystal mass from seeds, m_c^n signifies the crystal mass from nuclei, and m_c^{tot} signifies the total crystal mass from both seeds and nuclei.
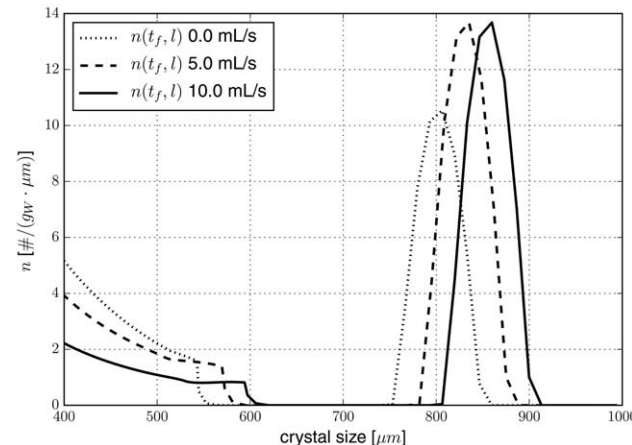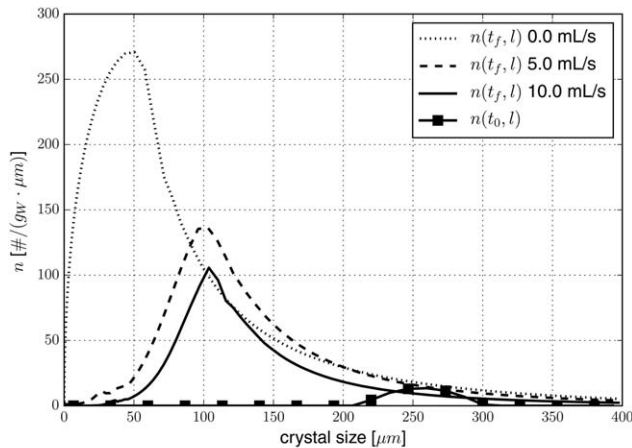
computational time is required for solving the MPC at each sampling time than is required when using the moment model. To circumvent this issue in a practical implementation, one could implement the second control action in the prediction horizon from the MPC solution at the previous sampling time.

Figures 12–14 show input and state profiles obtained by controlling the batch crystallization process under MPC for three values of $\dot{V}_{sp,\text{out}}$ (0, 5 and 10 $\frac{\text{mL}}{\text{s}}$). The case with $\dot{V}_{sp,\text{out}} = 0$ does not include the fines dissolution tank and is simulated according to Table 3. The optimal jacket temperature profiles computed by the MPC for the three different values of $\dot{V}_{sp,\text{out}}$ are shown in Figure 12. The MPC computes that the jacket profile that optimizes the objective function subject to the constraints should reach its final value earlier in the batch for the two cases that $\dot{V}_{sp,\text{out}}$ is nonzero than when it is zero. Under these manipulated input profiles, the dynamic profiles for the seed, nuclei and total crystal mass depicted in Figure 13 are obtained. Although the total mass from crystals is approximately the same for the three different values of $\dot{V}_{sp,\text{out}}$, operation for the cases with larger values of $\dot{V}_{sp,\text{out}}$ is associated with more crystal mass from seeds and less from nuclei in this figure. For example, the crystallizer under MPC with a fines dissolution loop with $\dot{V}_{sp,\text{out}} = 10$ $\frac{\text{mL}}{\text{s}}$ gives a 21.3% increase in

the crystal mass from the seeds compared to the crystallizer under MPC without a fines dissolution loop ($\dot{V}_{sp,\text{out}} = 0 \; \frac{\text{mL}}{\text{s}}$).

Figure 14 presents the PSD at the final batch time for all three values of $\dot{V}_{sp,\text{out}}$. To allow for better visualization of the results, the PSD has been split into two ranges corresponding to the top (the PSD from 0 to 400 μm crystal size) and bottom (the PSD from 400 to 1000 μm) plots in the figure. The initial PSD is also shown for the fines dissolution cases for comparison (the initial PSD for the case with $\dot{V}_{sp,\text{out}} = 0 \; \frac{\text{mL}}{\text{s}}$ is slightly different than that for the fines dissolution case but takes a similar shape, with seed crystals in a limited size range, and is omitted). The figures indicate that the crystallizer with a fines dissolution loop under optimal control has less crystals from nucleation at the end of the batch, with enhanced seed growth. For example, the average crystal size resulting from the seeds in the case that the fines dissolution loop is used with $\dot{V}_{sp,\text{out}} = 10 \frac{\text{mL}}{\text{s}}$ is approximately 6.8% larger than in the case without the fines dissolution loop. These results indicate that MPC can be an effective controller for a batch crystallization process for a racemic compound forming system, for various crystallizer designs, and can allow thermodynamic constraints, as well as constraints related to profit like yield, to be satisfied while an objective function related to crystal properties is optimized.

REMARK 7. *While a number of researchers have looked at MPC for crystallization, the novelty of this work is the focus on enantiomer systems and specifically on using thermodynamic data for a racemic compound forming system to develop constraints and an operating procedure for MPC that is based on solution thermodynamics. The two enantiomers of a racemic compound forming system have many identical properties and thus crystallizing a single enantiomer, as is often desirable in industry, poses challenges that are not observed for other types of systems (e.g., nonenantiomeric). First, the solution must be pre-enriched in the desired enantiomer, and second, the solution thermodynamics must be carefully understood and exploited during the batch operation to prevent crystals of the counter enantiomer from forming by maintaining the temperature and composition within a required range (which changes as the temperature changes). This work develops a methodology for achieving the desired enantioseparation while allowing product properties related to process economics to be optimized by exploiting ternary diagrams and solution thermodynamic data in the design of a controller for the batch process. The focus is not on the specific trajectories obtained during the crystallization operation, but rather on examining the use of MPC for a very different system thermodynamically than has been considered in other works on crystallization (e.g. Ref. 27, 51, 52) Furthermore, to the knowledge of the authors, MPC has not been examined for racemic compound forming systems in the literature, so the results of this work are also novel in showcasing the possible benefits of MPC compared to traditional cooling strategies in the literature for racemic compound forming systems such as linear cooling.*

Conclusions

In this work, a batch crystallization process for enantioseparation of racemic compound forming systems was considered. An operation and control strategy based on MPC for the crystallization process was developed that uses equations and information developed from a ternary diagram, and it was exemplified for the mandelic acid in water system. The MPC can optimize an objective function related to desired product characteristics while satisfying thermodynamic constraints (e.g., constraints on the minimum crystallizer temperature and yield) subject to a process model based on the solution thermodynamics data to allow for crystals of a single enantiomer to be obtained. The temperature profile in the crystallizer for the mandelic acid example was shown to be different under MPC than under a predefined linear cooling profile. A fines dissolution loop was shown to be effective at decreasing the number of crystals from nuclei for the process under MPC.

Literature Cited

1. Rentsch KM. The importance of stereoselective determination of drugs in the clinical laboratory. *J Biochem Biophys Methods*. 2002; 54:1–9.
2. McConathy J, Owens MJ. Stereochemistry in drug action. *Prim Care Companion J Clin Psychiatr*. 2003;5:70–73.
3. Nguyen LA, He H, Pham-Huy C. Chiral drugs: an overview. *Int J Biomed Sci*. 2006;2:85–100.
4. Raymond KW. *General Organic and Biological Chemistry: An Integrated Approach*, 3rd ed. Hoboken, NJ: Wiley, 2010.
5. Masterton WL, Hurley CN. *Chemistry: Principles and Reactions*, 5th ed. Belmont, CA: Thomson Brooks/Cole, 2006.
6. Brandenberger H, Maes RAA, editors. *Analytical Toxicology for Clinical, Forensic and Pharmaceutical Chemists*. Berlin, Germany: Walter de Gruyter, 1997.
7. Newmeyer MN, Concheiro M, da Costa JL, Flegel R, Gorelick DA, Huestis MA. Oral fluid with three modes of collection and plasma methamphetamine and amphetamine enantiomer concentrations after controlled intranasal l-methamphetamine administration. *Drug Testing Anal*. 2015;7:877–883.
8. Olliaro P, Delgado-Romero P, Keiser J. The little we know about the pharmacokinetics and pharmacodynamics of praziquantel (racemate and R-enantiomer). *J Antimicrobial Chemotherapy*. 2014;69: 863–870.
9. Yang X, Wong SY, Bwambok DK, Atkinson MBJ, Zhang X, Whitesides GM, Myerson AS. Separation and enrichment of enantiopure from racemic compounds using magnetic levitation. *Chem Commun*. 2014;50:7548–7551.
10. Pálovics E, Faigl F, Fogassy E. Separation of the mixtures of chiral compounds by crystallization. In Mastai Y, editor, *Advances in Crystallization Processes*. InTech, 2012. DOI:10.5772/33592.
11. Karamertzanis PG, Anandamanoharan PR, Fernandes P, Cains PW, Vickers M, Tocher DA, Florence AJ, Price SL. Toward the computational design of diastereomeric resolving agents: an experimental and computational study of 1-phenylethylammonium-2-phenylacetate derivatives. *J Phys Chem B*. 2007;111:5326–5336.
12. Mao S, Zhang Y, Rohani S, Ray AK. Kinetics of (R, S)-and (R)-mandelic acid in an unseeded cooling batch crystallizer. *J Crystal Growth*. 2010;312:3340–3348.
13. Subramanian G. editor. *Chiral Separation Techniques: A Practical Approach*, 3rd ed. Weinheim, Germany: Wiley-VCH, 2007.
14. Lorenz H, Seidel-Morgenstern A. Processes to separate enantiomers. *Angew Chem Int Ed Engl*. 2014;53:1218–1250.
15. A. S. Myerson, editor. *Handbook of Industrial Crystallization*, 2nd ed. Boston, MA: Butterworth-Heinemann, 2002.
16. Shekunov BY, York P. Crystallization processes in pharmaceutical technology and drug delivery design. *J Crystal Growth*. 2000;211:122–136.
17. Jacques J, Collet A, Wilen SH. *Enantiomers, Racemates, and Resolutions*. New York: Wiley, 1981.
18. Busch KW, Busch MA, editors. *Chiral Analysis*. Amsterdam, The Netherlands: Elsevier, 2006.
19. Kaspereit M. Separation of enantiomers by a process combination of chromatography and crystallisation. PhD thesis, Otto-von-Guericke-Universität Magdeburg, 2006.

20. Lim B-G, Ching C-B, Tan RBH, Ng S-C. Recovery of (-)-praziquantel from racemic mixtures by continuous chromatography and crystallisation. *Chem Eng Sci*. 1995;50:2289–2298.
21. Lorenz H, Sheehan P, Seidel-Morgenstern A. Coupling of simulated moving bed chromatography and fractional crystallisation for efficient enantioseparation. *J Chromatogr A*. 2001;908:201–214.
22. Ströhlein G, Schulte M, Strube J. Hybrid processes: design method for optimal coupling of chromatography and crystallization units. *Sep. Sci. Technol*. 2003;38:3353–3383.
23. Amanullah M, Mazzotti M. Optimization of a hybrid chromatography-crystallization process for the separation of Tröger's base enantiomers. *J Chromatogr A*. 2006;1107:36–45.
24. Mao S. Chiral separation of racemic mandelic acid by the coupling crystallization process and simulated moving bed technology. PhD thesis, The University of Western Ontario, 2012.
25. Swernath S. Design and control of combined chemical processes for the production of pure enantiomers. PhD thesis, Otto-von-Guericke-Universität Magdeburg, 2013.
26. Nayhouse M, Tran A, Kwon JS-I, Crose M, Orkoulas G, Christofides PD. Modeling and control of ibuprofen crystal growth and size distribution. *Chem Eng Sci*. 2015;134:414–422.
27. Patience DB, Dell'Orco PC, Rawlings JB. Optimal operation of a seeded pharmaceutical crystallization with growth-dependent dispersion. *Org Process Res Dev*. 2004;8:609–615.
28. Diab S, Gerogiorgis DI. Process modeling, simulation, and technoeconomic evaluation of separation solvents for the continuous pharmaceutical manufacturing (CPM) of diphenhydramine. *Org Process Res Dev*. 2017;21:924–946.
29. Lorenz H, Seidel-Morgenstern A. Binary and ternary phase diagrams of two enantiomers in solvent systems. *Thermochimica Acta*. 2002;382:129–142.
30. Lorenz H, Sapoundjiev D, Seidel-Morgenstern A. Solubility equilibria in chiral systems and their importance for enantioseparation. *Eng Life Sci*. 2003;3:132–136.
31. Worlitschek J. Monitoring, modeling and optimization of batch cooling crystallization. PhD thesis, Swiss Federal Institute of Technology Zurich, 2003.
32. Kaemmerer H, Jones MJ, Lorenz H, Seidel-Morgenstern A. Selective crystallisation of a chiral compound-forming system - solvent screening, SLE determination and process design. *Fluid Phase Equilibria*. 2010;296:192–205.
33. Kwon JS-I, Nayhouse M, Christofides PD, Orkoulas G. Modeling and control of crystal shape in continuous protein crystallization. *Chem Eng Sci*. 2014;107:47–57.
34. Chiu TY, Christofides PD. Robust control of particulate processes using uncertain population balances. *AIChE J*. 2000;46:266–280.
35. Shi D, El-Farra NH, Li M, Mhaskar P, Christofides PD. Predictive control of particle size distribution in particulate processes. *Chem Eng Sci*. 2006;61:268–281.
36. Chianese A, Kramer HJM, editors. *Industrial Crystallization Process Monitoring and Control*. Weinheim, Germany: Wiley-VCH, 2012.
37. Randolph AD, Larson MA. *Theory of Particulate Processes: Analysis and Techniques of Continuous Crystallization*. Academic Press, San Diego, California, 1988.
38. Angelov I, Raisch J, Elsner MP, Seidel-Morgenstern A. Optimal operation of enantioseparation by batch-wise preferential crystallization. *Chem Eng Sci*. 2008;63:1282–1292.
39. Zhang Y, Mao S, Ray AK, Rohani S. Nucleation and growth kinetics of (R)-mandelic acid from aqueous solution in the presence of the opposite enantiomer. *Cryst Growth Des*. 2010;10:2879–2887.
40. Qamar S, Mukhtar S, Seidel-Morgenstern A, Elsner MP. An efficient numerical technique for solving one-dimensional batch crystallization models with size-dependent growth rates. *Chem Eng Sci*. 2009;64:3659–3667.
41. Kumar S, Ramkrishna D. On the solution of population balance equations by discretization III. Nucleation, growth and aggregation of particles. *Chem Eng Sci*. 1997;52:4659–4679.
42. Walther A, Griewank A. Getting started with ADOL-C. In Naumann U, Schenk O, editors, *Combinatorial Scientific Computing*. Boca Raton, Florida: CRC Press, 2012:181–202.
43. Carpenter MH, Kennedy CA. Fourth-order 2N-storage Runge-Kutta schemes. Technical report, NASA, Technical Memorandum 109112, 1994.
44. Williamson JH. Low-storage Runge-Kutta schemes. *J Comput Phys*. 1980;35:48–56.
45. Kwon JS-I, Nayhouse M, Orkoulas G, Christofides PD. Crystal shape and size control using a plug flow crystallization configuration. *Chem Eng Sci*. 2014;119:30–39.
46. Codan L, Eckstein CF, Mazzotti M. Growth kinetics of S-mandelic acid in aqueous solutions in the presence of R-mandelic acid. *Crystal Growth Design*. 2013;13:652–663.
47. Mullin JW. *Crystallization*, 4th ed. Woburn, MA: Butterworth-Heinemann, 2001.
48. Christofides PD. *Model-Based Control Of Particulate Processes*. Dordrecht, The Netherlands: Kluwer Academic Publishers, 2002.
49. Wächter A, Biegler LT. On the implementation of an interior-point filter line-search algorithm for large-scale nonlinear programming. *Math Program*. 2006;106:25–57.
50. Miller SM, Rawlings JB. Model identification and control strategies for batch cooling crystallizers. *AIChE J*. 1994;40:1312–1327.
51. Kwon JS-I, Nayhouse M, Orkoulas G, Ni D, Christofides PD. Run-to-run-based model predictive control of protein crystal shape in batch crystallization. *Ind Eng Chem Res*. 2015;54:4293–4302.
52. Tseng Y-T, Ward JD. Comparison of objective functions for batch crystallization using a simple process model and Pontryagin's minimum principle. *Comput Chem Eng*. 2017;99:271–279.